JCTC Journal of Chemical Theory and Computation

pubs.acs.org/JCTC Review

A Critical Assessment on Calculating Vibrational Spectra in Nanostructured Materials

Alexander E. J. Hoffman, Wim Temmerman, Emma Campbell, Alessandro Ali Damin, Ines Lezcano-Gonzalez, Andrew M. Beale, Silvia Bordiga, Johan Hofkens, and Veronique Van Speybroeck*

Cite This: J. Chem. Theory Comput. 2024, 20, 513−531 Read Online

ABSTRACT: Vibrational spectroscopy is an omnipresent spectroscopic technique to characterize functional nanostructured materials such as zeolites, metal−organic frameworks (MOFs), and metal−halide perovskites (MHPs). The resulting experimental spectra are usually complex, with both low-frequency framework modes and high-frequency functional group vibrations. Therefore, theoretically calculated spectra are often an essential element to elucidate the vibrational fingerprint. In principle, there are two possible approaches to calculate vibrational spectra: (i) a static approach that approximates the potential energy surface (PES) as a set of independent harmonic oscillators and (ii) a dynamic approach that explicitly samples the PES around equilibrium by integrating Newton's equations of motions. The dynamic approach considers anharmonic and temperature effects and provides a more genuine representation of materials at true operating conditions; however, such simulations come at a substantially increased computational cost. This is certainly true when forces and energy evaluations are performed at the quantum mechanical level. Molecular dynamics (MD) techniques have become more established within the field of computational chemistry. Yet, for the prediction of infrared (IR) and Raman spectra of nanostructured materials, their usage has been less explored and remain restricted to some isolated successes. Therefore, it is currently not *a priori* clear which methodology should be used to accurately predict vibrational spectra for a given system. A comprehensive comparative study between various theoretical methods and experimental spectra for a broad set of nanostructured materials is so far lacking. To fill this gap, we herein present a concise overview on which methodology is suited to accurately predict vibrational spectra for a broad range of nanostructured materials and formulate a series of theoretical guidelines to this purpose. To this end, four different case studies are considered, each treating a particular material aspect, namely breathing in flexible MOFs, characterization of defects in the rigid MOF UiO-66, anharmonic vibrations in the metal−halide perovskite $CsPbBr_3$, and guest adsorption on the pores of the zeolite H-SSZ-13. For all four materials, in their guest- and defect-free state and at sufficiently low temperatures, both the static and dynamic approach yield qualitatively similar spectra in agreement with experimental results. When the temperature is increased, the harmonic approximation starts to fail for $CsPbBr_3$ due to the presence of anharmonic phonon modes. Also, the spectroscopic fingerprints of defects and guest species are insufficiently well predicted by a simple harmonic model. Both phenomena flatten the potential energy surface (PES), which facilitates the transitions between metastable states, necessitating dynamic sampling. On the basis of the four case studies treated in this Review, we can propose the following theoretical guidelines to simulate accurate vibrational spectra of functional solid-state materials: (i) For nanostructured crystalline framework materials at low temperature, insights into the lattice dynamics can be obtained using a static approach relying on a few points on the PES and an independent set of harmonic oscillators. (ii) When the material is evaluated at higher temperatures or when additional complexity enters the system, *e.g.*, strong anharmonicity, defects, or guest species, the harmonic regime breaks down and dynamic sampling is required for a correct prediction of the phonon spectrum. These guidelines and their illustrations for prototype material classes can help experimental and theoretical researchers to enhance the knowledge obtained from a lattice dynamics study.

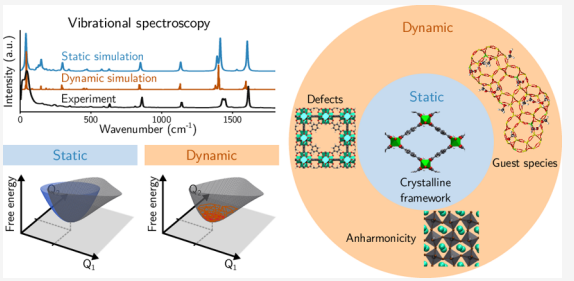

INTRODUCTION

The continuous challenge to find technological solutions for present-day problems stimulates the design of new functional nanostructured materials. Thanks to advanced synthetic algorithms, such materials are now being developed at a high pace. Within this paper, we focus on the simulation of

Received: August 27, 2023
Revised: November 30, 2023
Accepted: December 5, 2023
Published: December 29, 2023

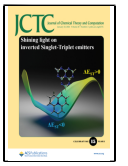

https://doi.org/10.1021/acs.jctc.3c00942
J. Chem. Theory Comput. 2024, 20, 513−531

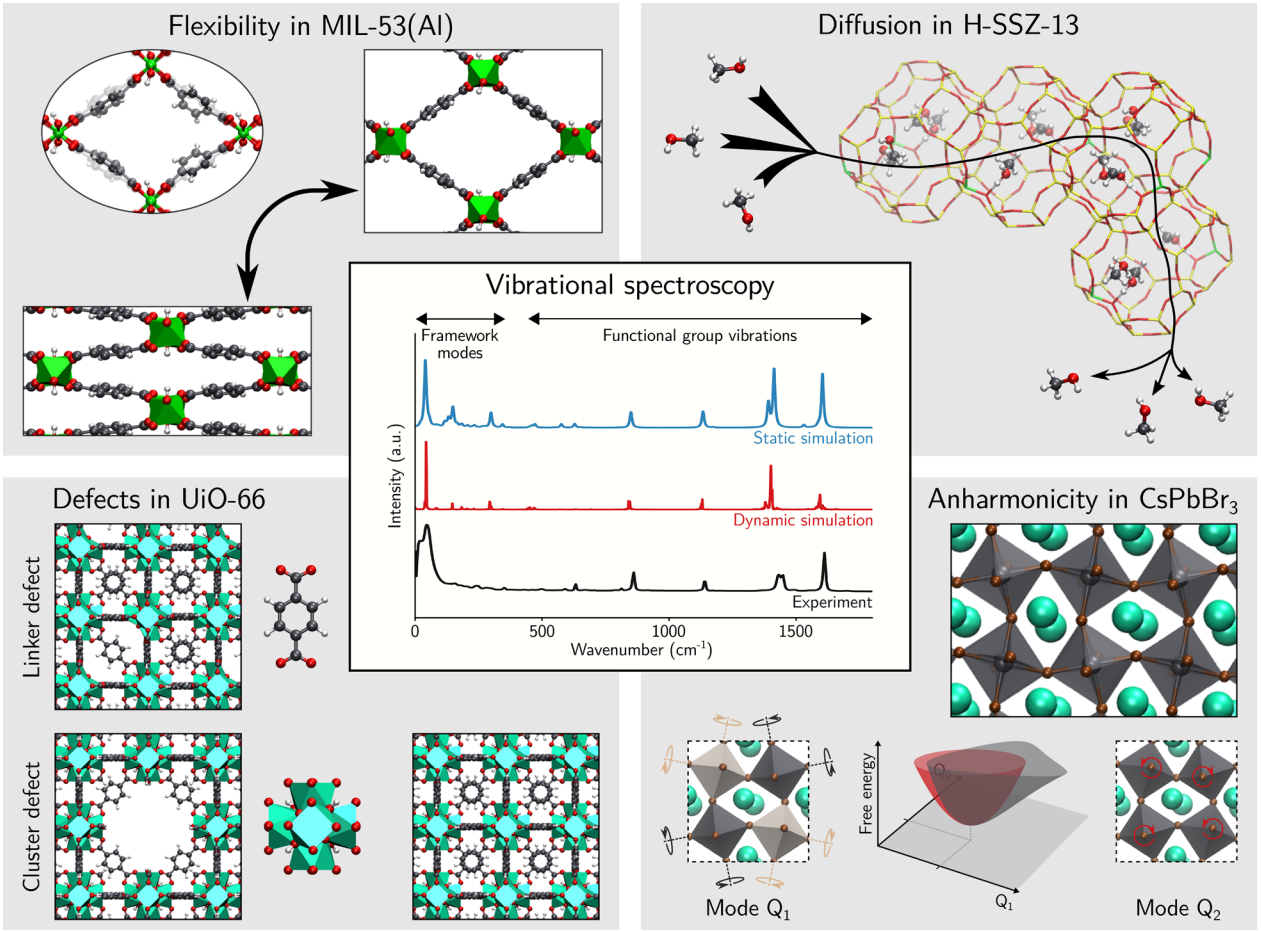

Figure 1. Overview of the four different case studies treated in this work.

vibrational spectra of three specific functional nanostructured material types, namely zeolites, metal−organic frameworks (MOFs), and metal−halide perovskites (MHPs). This choice is inspired to cover a broad range of nanostructured materials with different features, which should allow the formulation of general guidelines on how one can calculate vibrational spectra of these materials that align with experimental observations. In this contribution, periodic density functional theory is applied to study different properties in nanostructured materials. Surface and/or interfacial effects on phonon properties (as discussed by, *e.g.*, Dzhagan et al.[1]) are not accounted for and were considered outside the scope of this work. As will become clear, depending on the specific features of the materials, *i.e.*, having defects or not, having pores with or without inclusion of guest molecules, *etc.*, other methodologies are necessary to accurately predict vibrational spectra.

Three classes of materials are investigated within this Review, as shortly introduced hereafter. First, zeolites are considered, which are inorganic microporous crystalline frameworks that are already routinely employed in chemical industry because they can increase the catalytic efficiency of chemical processes.[2,3] This is, for example, of interest in the production of olefins from methanol[4] and the reduction of NO_x from exhaust gases.[5,6] Furthermore, their porosity is beneficial in gas separation applications.[7] Zeolites can exist under various topologies[8] and with a wide-range of acid site distributions,[9] affecting their catalytic and separation performances. Second, MOFs are examined, which are a more recent class of nanoporous and/or microporous crystalline materials.[10−12] They are formed by inorganic polynuclear clusters connected by organic linkers. Within the concept of reticular chemistry, these two types of building blocks may be altered, allowing the functionalization of the material.[13] This renders MOFs versatile materials with many different potential applications in the fields of heterogeneous catalysis,[14] gas separation,[15] drug delivery,[16] chemical sensing,[17] *etc.* Depending on the specific framework topology and building blocks, MOFs may exhibit framework flexibility or not.[18,19] Flexible MOFs are characterized by their potential to switch phases upon exposure to external stimuli such as pressure, temperature, guest adsorption, *etc.* Vibrational spectra may be critically dependent on the particular phase of the MOF;[20,21] in this sense, both flexible and rigid MOFs are considered in this Review, as schematically shown in Figure 1. Lastly, MHPs are taken into account, which are a set of emerging functional nanostructured materials.[22,23] They have a structural formula of ABX_3 in which A represents an organic or inorganic monovalent cation, B acts for a divalent metal cation, and X takes the form of a halide anion. They exhibit suitable electronic properties, turning them into promising materials within solar cells or other energy conversion devices.[24,25] In contrast to zeolites and MOFs, they do not show porosity, but similar to flexible MOFs they can undergo phase transformations under particular conditions to which they are exposed. They are thus categorized as polymorphic materials.

https://doi.org/10.1021/acs.jctc.3c00942
J. Chem. Theory Comput. 2024, 20, 513−531

In order to assess the potential application of functional nanostructured materials in new or existing technologies, these materials need to be properly characterized. In that respect, a broad range of experimental spectroscopic techniques are available.[26−29] Vibrational spectroscopy has proven to be a very strong characterization technique, as it allows the investigation of both dynamical and structural features through analysis of the phonon modes with frequencies in the infrared (IR) range.[30−32] Low-frequency phonon modes or terahertz vibrations, involving collective displacements within the entire material, govern the lattice dynamics. These low-frequency phonon modes yield the largest contributions to the vibrational entropy and, hence, affect the thermal stability of the material, in some cases inducing structural phase transformations.[33−37] High-frequency vibrations, in the mid-IR range of the spectrum, determine the local bond strength. Consequently, high-frequency vibrations provide information on the presence and structure of specific functional groups.[30,32,38] IR and Raman spectroscopy are the most frequently used vibrational spectroscopic techniques. Through the absorption or scattering of light, they probe the change in the dipole moment or the polarizability, respectively, and are, hence, subject to selection rules, meaning that not all phonon modes will be detected. Other vibrational spectroscopic techniques, such as sum-frequency generation (SFG)[39] and inelastic neutron scattering (INS),[40] exist that depend on different or no selection rules, allowing the study of complementary phonon modes.

The interpretation of experimental vibrational spectra of nanostructured materials is often not trivial. This is certainly true for low-frequency vibrations, which rely on weak forces and often span a broad frequency range. Therefore, they can no longer be easily interpreted purely based on chemical insight.[41,42] High-frequency vibrations can be associated with isolated bonds and are usually characteristic for specific functional groups; as a result, they exhibit sharp spectral bands centered around a characteristic frequency due to strong bonds. Nevertheless, for complex nanostructured materials, their interpretation might not always be trivial due to overlapping bands. Furthermore, the presence of defects may influence the character and frequency of the phonon modes.[43] Also, the identification of multiple guest species within porous framework materials can become cumbersome when their characteristic vibrational fingerprints overlap.[44] Theoretical calculations are quintessential to assist in the assignment of phonon modes. In addition, observations from simulations provide detailed molecular-level insight, turning them into an indispensable characterization tool for the material under study.[42,45−48] However, to obtain a reliable prediction of spectra, it is important to employ a proper theoretical model that is representative for the system of interest.

The modeling of a material typically consists of four different steps.[49] At first instance, a realistic atomistic representation of the system needs to be defined. Second, the forces between the atoms should be evaluated by constructing the potential energy surface (PES), which defines the equilibrium configuration and the surrounding states in configuration space. Once a description of the PES is available, the vibrational properties can be determined in the last two steps. In step three, the PES should be sampled, which is possible through different approaches. One can choose a simple harmonic sampling of the PES around its equilibrium configuration, referred to as the static or local approach, in which the phonon modes appear as solutions of harmonic oscillators. Although this harmonic approximation has a low computational cost and gives direct access to the phonon modes, it only samples the equilibrium state at 0 K and neglects temperature and anharmonic effects. The latter can be dealt with by including anharmonic corrections in the model, but this increases the computational cost significantly.[50−52] A more realistic sampling of the PES is obtained via molecular dynamics (MD) simulations. By solving Newton's equations of motion at subsequent time steps, it is possible to sample the true shape of the PES around its equilibrium configuration. This has the advantage that temperature effects and (a certain amount of) anharmonicity are accounted for. However, the successive evaluation of the molecular forces together with the necessity of long MD trajectories, required to reach a converged sampling of the PES, increases the computational cost.[53] Moreover, during an MD run, all phonon modes are excited simultaneously. Therefore, they are no longer directly accessible but follow only after additional spectral analysis.[54]

Once the PES has been sampled, the actual vibrational properties can be determined in the final step. Several thermal and mechanical properties, such as the thermal expansion coefficient, the heat capacity, and the bulk modulus, follow directly or indirectly from the phonon mode frequencies.[55,56] Other vibrational properties need additional theoretical input before they can be predicted. The theoretical prediction of IR intensities, for example, requires the calculation of the dipole moment, which corresponds to the derivative of the potential energy to the external electric field.[57] The central property in the prediction of Raman intensities is the polarizability tensor, which corresponds to the derivative of the dipole moment or the second-derivative of the potential energy to the external electric field.[57] Similarly, specific molecular properties are needed to predict intensities of other vibrational spectra such as SFG[58,59] and INS.[40]

To date, it is not clear *a priori* which theoretical approach could be employed for a given nanostructured material to accurately predict and explain the experimentally observed vibrational fingerprints. The quality of the theoretical model can strongly depend on several factors, such as the flexibility of the framework, the presence of defects, the manifestation of anharmonic phonon modes, the presence of guest species, *etc.* In this Review, the performance of both static and dynamic simulation techniques to calculate vibrational properties of functional nanostructured materials is assessed by comparing theoretical and experimental spectra. Furthermore, some calculated bulk properties, such as the bulk modulus, the thermal expansion coefficient, and the heat capacity, which depend on the phonon modes, will also be compared with experimental reference values. For that purpose, four different case studies will be highlighted, each treating a specific material's aspect (see Figure 1). A first case study considers the flexible MOF MIL-53(Al).[60] It undergoes a breathing transition between a closed pore and a large pore phase in which the low-frequency phonon modes contribute to the breathing mechanism.[20] Second, the case of the rigid MOF UiO-66 will be treated.[61] Although UiO-66 is a very stable MOF, it often contains defects that have an impact on its vibrational properties.[43] Next, the MHP $CsPbBr_3$ will be investigated, which exhibits strong anharmonic character.[62,63] Finally, the influence of guest species within a porous framework on the vibrational fingerprints will also be studied. In that regard, the vibrational properties of H-SSZ-13, a prototypical zeolite used in catalytic applications, will be

https://doi.org/10.1021/acs.jctc.3c00942
J. Chem. Theory Comput. 2024, 20, 513−531

predicted when it is loaded with methanol or ethanol.[44] The aforementioned case studies naturally lead to the formulation of general guidelines, valid for a wide range of nanostructured materials, to perform accurate calculations of vibrational properties. This will help experimental and theoretical researchers to gain insight in a specific nanostructured material.

METHODOLOGICAL ASPECTS OF CALCULATING VIBRATIONAL PROPERTIES

Sampling the PES. Following the Born−Oppenheimer approximation,[64] the time-independent electronic Schrödinger equation can be written as follows:

$$\hat{\mathcal{H}}_e(\mathbf{r}, \mathbf{R})\Psi_e(\mathbf{r}, \mathbf{R}) = \mathcal{V}(\mathbf{R})\Psi_e(\mathbf{r}, \mathbf{R}) \quad (1)$$

Here $\hat{\mathcal{H}}_e$ represents the electronic Hamiltonian operator and Ψ_e is the electronic wave function of the ground state. They are both a function of the electronic coordinates $\mathbf{r}$ but depend only parametrically on the nuclear coordinates $\mathbf{R}$. For simplicity, the spin dependency is incorporated in the electronic coordinates. The solution of this eigenvalue equation yields the electronic energy $\mathcal{V}$, which becomes a function of the nuclear coordinates. The finally obtained multidimensional function $\mathcal{V}$, in terms of the nuclear coordinates, yields the potential energy surface on which the dynamics of the nuclei can be evaluated.

Several methods exist to calculate the PES of the system, which are all approximate for systems having more than one electron due to the presence of electron−electron interaction.[65−68] Density functional theory (DFT) is nowadays the method of choice to determine the electronic structure thanks to its attractive computational cost and the ability to include electron correlation if a proper exchange-correlation functional is chosen.[69,70] Despite its success, DFT can, with the currently available computational resources, treat systems in the nanometer length scale having maximally a few thousand atoms.[71−73] For larger systems, more crude approximations are necessary. An often applied methodology is the usage of classical force fields where the interactions between the different atoms and functional groups are described by analytical functions with predefined force constants.[74−77] However, in the case of vibrational spectroscopy, this makes the phonon modes strongly dependent on the applied force field. Furthermore, due to the lack of information on the electronic structure, derived properties such as the dipole moment and polarizability can no longer be straightforwardly obtained, and extensions to the force field model are required to be able to calculate them.[78−81] Recently, the gap between electronic structure and classical force field methods is being bridged by machine learning (ML) techniques, which allow the use of ML potentials (MLPs) at the computational cost of regular force field methods with the accuracy of first-principle methods.[82−85] However, for the calculation of IR and Raman spectra, special MLPs need to be developed that also take into account the electron density, which is an area that is currently being explored[86−88] and certainly not yet available for the complex materials under study in this account. Within this contribution, we restrict ourselves to methodologies where the PES is described by means of DFT.

Irrespective of the applied method to calculate the potential energy of a molecular configuration, the PES can be sampled using different approaches. In the following, the two most frequently applied techniques in the field of computational vibrational spectroscopy will be highlighted: the harmonic approximation and MD (see Figure 2).

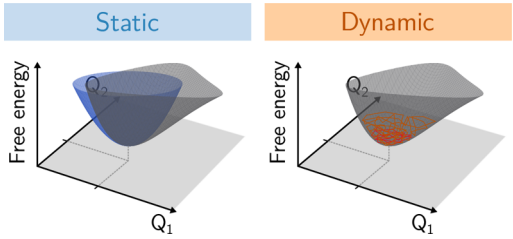

Figure 2. Illustration of the static and dynamic approaches to sampling the PES.

Harmonic Approximation. Around its equilibrium configuration, $\boldsymbol{R}_0$, the PES can be approximated by its Taylor expansion up to second order:

$$\mathcal{V}(\boldsymbol{R}) = \mathcal{V}(\boldsymbol{R}_0) + \sum_i q_i \frac{\partial \mathcal{V}}{\partial q_i}(\boldsymbol{R}_0) + \frac{1}{2}\sum_{i,j} q_i q_j \frac{\partial^2 \mathcal{V}}{\partial q_i \partial q_j}(\boldsymbol{R}_0) + O(\boldsymbol{q}^3) \quad (2)$$

where $\boldsymbol{q} = \boldsymbol{R} - \boldsymbol{R}_0$ corresponds to the displacement vector. In equilibrium, there are no forces working on the system and, therefore, the first-order derivatives of the potential energy with respect to the displacement equal zero, *i.e.*, $\frac{\partial \mathcal{V}}{\partial q_i}(\boldsymbol{R}_0)=0$. In the harmonic approximation, the third- and higher-order terms are neglected. The only remaining terms, apart from the constant potential energy at equilibrium, are the ones containing the second-order derivatives of the potential energy with respect to the displacement, which correspond to the matrix of force constants and are referred to as the Hessian matrix:

$$\mathrm{H}_{ij} = \frac{\partial^2 \mathcal{V}}{\partial q_i \partial q_j}(\boldsymbol{R}_0) \quad (3)$$

For periodic systems, the size of the Hessian becomes infinitely large. Therefore, the dynamical matrix, $\mathbf{D}(\boldsymbol{k})$, is introduced, which is the mass-weighted discrete Fourier transform of the Hessian. The dynamical matrix is a function of the wavenumber $\boldsymbol{k}$ and has a dimension of $3N \times 3N$, with N being the number of atoms in the unit cell. In the harmonic approximation, phonon modes appear as the eigenvectors of the dynamical matrix and their vibrational frequencies as the square root of the eigenvalues:

$$\mathbf{D}(\boldsymbol{k})\mathbf{Q}_n(\boldsymbol{k}) = \omega_n^2(\boldsymbol{k})\mathbf{Q}_n(\boldsymbol{k}) \quad (4)$$

The dynamical matrix and its corresponding phonon modes are uniquely defined in the entire first Brillouin zone. However, as only phonon modes in the center of the Brillouin zone (Γ-point) may exhibit IR and/or Raman activity, we will consider $\boldsymbol{k} = \mathbf{0}$ in the following. In case anharmonicities are important, there are specific ways to go beyond the harmonic approximation for nanostructured materials. On the one hand, a volume dependence of the phonon modes can be introduced by determining the Hessian and its corresponding normal modes at different volumes, which is referred to as the quasi-harmonic approximation (QHA).[89,90] This allows the investigation of thermal and mechanical properties depending on phonon modes. On the other hand, it is possible to add higher-order terms in the expression of the Taylor expansion.[51]

https://doi.org/10.1021/acs.jctc.3c00942
J. Chem. Theory Comput. 2024, 20, 513−531

Several approaches have been proposed that take into account these anharmonic corrections,[52,91−93] such as the vibrational self-consistent field (VSCF),[94,95] the vibrational configuration interaction (VCI),[96,97] the vibrational perturbation theory (VPT),[98−100] and the vibrational coupled-cluster (VCC)[101,102] methods. Although the above-mentioned approaches can significantly improve the prediction of phonon modes, especially in anharmonic systems, this comes with an increased computational load. Therefore, they have, so far, mostly been applied on materials with a small unit cell.[52]

Molecular Dynamics (MD). The harmonic approximation and its anharmonic extensions are static or local approaches in the sense that the PES is determined around the equilibrium configuration, with fixed positions of the nuclei determined after optimization at 0 K. In contrast, molecular dynamics (MD) techniques rely on dynamic sampling, where the nuclei are able to move on the actual PES and visit different configurations in the vicinity of the equilibrium. The sequence of nuclear configurations are obtained by solving Newton's equations of motion, which requires the calculation of the forces working on a specific configuration at time t from which the acceleration of the nuclei can be obtained:

$$\mathcal{M}_i \frac{\partial^2 R_i(t)}{\partial t^2} = -\nabla_i \mathcal{V}(\boldsymbol{R}(t)) \tag{5}$$

where $\mathcal{M}_i$ is the mass of the nucleus with position $\boldsymbol{R}_i$ and $\nabla\mathcal{V}(\boldsymbol{R}(t))$ is the gradient of the potential energy of the configuration visited at time t. Via numerical integration, for example with the velocity Verlet algorithm, the nuclear positions at time $t + \Delta t$ can be obtained. Through evaluation of the equations of motion at subsequent timesteps, a physical path between different configurations is constructed and, gradually, the PES is explored. Besides the advantage that MD can sample configurations away from equilibrium and explicitly take the anharmonic shape of the PES into account, it is also possible to control parameters such as temperature and pressure via thermostats and barostats, respectively, to allow sampling of the PES at the correct experimental conditions.[103,104] However, MD simulations are computationally more expensive, as the potential energy needs to be calculated at every time step and for many different configurations. In this regard, efficient algorithms have been developed that make use of information obtained at previous time steps, reducing the computational load to some extent.[105] Furthermore, individual phonon modes are not readily accessible from an MD simulation, as all modes are excited simultaneously. They should be extracted from an MD run via spectral analysis techniques, which require sufficiently long simulation times in order to reach convergence.[106] Finally, the classical Newton equations of motion neglect the quantum character of the nuclei, which becomes important for light nuclei such as hydrogen and at low temperatures. To correctly sample the PES in these situations, these nuclear quantum effects should be accounted for via techniques such as path integral MD, again increasing the computational cost.[107] Within this contribution we will test both the harmonic approximation- and MD-based approaches. However, nuclear quantum effects are not explicitly treated, as this would necessitate a significant increase of computational resources.

Derivation of Vibrational Properties. Once the PES has been sampled, either locally by means of the harmonic approximation or by also including nonlocal effects via MD techniques, vibrational properties can be determined. In the following, the calculation of IR and Raman spectra via static (or local) and dynamic approaches will be discussed. Moreover, the procedure to obtain thermal and mechanical properties using the QHA will be highlighted.

IR Spectra. Phonons can interact with electromagnetic radiation by absorbing IR light, giving rise to the IR spectrum. This interaction can be described by a perturbation of the nuclear Hamiltonian $\hat{\mathcal{H}}_N$:

$$\hat{\mathcal{H}}'_N = -\hat{\boldsymbol{M}}\cdot\boldsymbol{E} \tag{6}$$

in which $\hat{\boldsymbol{M}}$ represents the dipole moment operator of the system and $\boldsymbol{E}$ corresponds to the external electric field due to the electromagnetic radiation. Based on quantum mechanical considerations, an expression for the total absorption can be obtained. The derivation will be summarized in the following. We refer to section S1.1 in the Supporting Information for a step by step derivation. The total absorption at a certain frequency depends on the probability that a transition between vibrational states occurs. Therefore, Fermi's golden rule can be applied, eventually yielding the following expression for the absorbance A as a function of frequency:

$$A(\omega) \sim \omega(1-e^{-\hbar\omega/k_B T})\sum_f \sum_i \rho_i |\langle f|\hat{\boldsymbol{M}}|i\rangle\cdot\boldsymbol{E}|^2 \delta(\omega_{fi} - \omega) \tag{7}$$

Here, $\hbar$ and k_B are Planck's constant divided by 2π and Boltzmann's constant, respectively. T is the temperature, i and f represent the initial and final state, and ρ_i is the probability to encounter initial state i. The evaluation of the sums over the initial and final states is carried out differently when a static or a dynamic approach is applied. In the former approach, the double harmonic approximation allows one to expand the dipole moment operator in a Taylor expansion up to first order in the phonon modes:

$$A(\omega) \sim \omega(1 - e^{-\hbar\omega/k_B T})\sum_f \sum_i \rho_i \left| \left\langle f \middle| \boldsymbol{M}_0 + \sum_n \left(\frac{\partial \boldsymbol{M}}{\partial Q_n}\right)_0 \widehat{Q}_n \middle| i \right\rangle \cdot \boldsymbol{E} \right|^2 \delta(\omega_{fi} - \omega) \tag{8}$$

where $\widehat{Q}_n$ is the normal mode operator of mode n. The permanent dipole moment $\boldsymbol{M}_0$ does not operate on the orthonormal vibrational eigenstates and, hence, the term vanishes. Following the properties of harmonic oscillator eigenstates, applying the Boltzmann distribution law to estimate ρ_i, and upon rotational averaging, the absorbance of a specific phonon mode n is given by

$$A_n(\omega) \sim \left(\frac{\partial \boldsymbol{M}}{\partial Q_n}\right)_0^2 \delta(\omega_n - \omega) \tag{9}$$

$$\sim (\mathbf{Z}\boldsymbol{Q}_n)_0^2 \delta(\omega_n - \omega) \tag{10}$$

$\mathbf{Z}$ is the notation for the Born effective charge (BEC) tensor, which contains the derivatives of the dipole moment with respect to the Cartesian coordinates. The BEC, as a second-order derivative of the energy with respect to the electric field

https://doi.org/10.1021/acs.jctc.3c00942
J. Chem. Theory Comput. 2024, 20, 513−531

and the Cartesian coordinates, can be efficiently calculated via a finite difference[108] or linear response[109] approach.

In the finite differences approach, the atoms in the system are first displaced along the independent directions to calculate the forces from single point calculations. Next, the second-order force constants can be obtained with any scheme of finite differences. Supercells are required to capture long-wavelength phonons, and phonons are calculated exactly at the wave vectors commensurate with the supercell.

Alternatively, the linear response of the electronic charge density can be calculated using the Kohn−Sham orbitals, requiring only calculations on the ground-state crystal. An advantage to this approach is that, in principle, the response to incommensurate wavevectors can be calculated without the construction of a supercell. Finite wave vector responses can be obtained within the primitive unit cell and thus the computational cost is reduced compared with the finite differences approach. However, some software packages can only calculate phonons with the linear response approach at the Γ-point and will, as with the finite differences approach, require supercells to calculate phonon dispersion relations. In both approaches, symmetry in the supercell can be exploited to reduce the computational load by limiting the number of single point calculations.

The static IR spectrum is thus characterized by several δ peaks. In order to increase the agreement with experiment, which is subject to temperature and imperfections, they are usually broadened by adding a line shape, typically Gaussian or Lorentzian.

In the dynamic approach, the Fourier transform of the Dirac δ function is introduced in eq 7, which allows one to rewrite the expression:

$$A(\omega) \sim \omega(1-e^{-\hbar\omega/k_B T}) \int_{-\infty}^{+\infty} \mathrm{d}t e^{-i\omega t} \langle \hat{\boldsymbol{M}}(0)\cdot\hat{\boldsymbol{M}}(t)\rangle_{\mathrm{qm}} \tag{11}$$

in which $\langle \hat{\boldsymbol{M}}(0)\cdot\hat{\boldsymbol{M}}(t)\rangle_{\mathrm{qm}}$ represents the quantum mechanical ensemble average of the autocorrelation function of the dipole moment. Consequently, by simply taking the Fourier transform of this autocorrelation function, the IR spectrum is immediately obtained. However, the ensemble average is usually obtained through classical MD calculations. In that case, in order to correct for the quantum character of the nuclei, a quantum correction factor needs to be taken into account. A natural choice is the so-called harmonic approximation,[110] which leads to the following expression for the absorbance:

$$A(\omega) \sim \omega^2 \int_{-\infty}^{+\infty} \mathrm{d}t e^{-i\omega t} \langle \boldsymbol{M}(0)\cdot\boldsymbol{M}(t)\rangle_{\mathrm{classic}} \tag{12}$$

Hence, the calculation of the IR spectrum via MD requires only the calculation of the dipole moment at subsequent time steps. Instead of using the autocorrelation of the dipole moment, the autocorrelation of the derivative of the dipole moment can also be applied. This leads to a similar expression as eq 12 in which ω^2 disappears due to properties of the Fourier transform. The absorbance obtained from an MD simulation is a continuous function of the frequency, which naturally possesses a line shape; as such, it is in principle not required to artificially broaden the IR spectrum. However, an additional line shape might still be applied to account for experimental features that are not considered in the theoretical model (*e.g.*, defects).

Raman Spectra. Besides absorption, phonons can also interact with light by scattering, which yields the Raman spectrum. Scattered light originates from the oscillating dipole moment, $\boldsymbol{m}$, induced through the external electric field $\boldsymbol{E}$:

$$\boldsymbol{m} = \boldsymbol{\alpha}\cdot\boldsymbol{E} \tag{13}$$

where $\boldsymbol{\alpha}$ represents the polarizability tensor. Analogous to the expressions for the absorbance, in which the dipole moment is the property of interest, the scattering intensity, I, for normal vibrational Raman scattering depends on the polarizability tensor. The full quantum mechanical derivation of the scattering intensity can be found in section S1.2 of the Supporting Information. The most important steps are highlighted here. The initial expression for the scattering intensity is given by

$$I(\omega) \sim \omega_s^4 \sum_f \sum_i \rho_i |\boldsymbol{E}^s\cdot\langle f|\hat{\alpha}|i\rangle\cdot\boldsymbol{E}|^2 \delta(\omega_{fi} - \omega) \tag{14}$$

in which ω_s and $\boldsymbol{E}^s$ are the frequency and electric field of the scattered light. $\hat{\alpha}$ corresponds to the operator form of the polarizability tensor. In contrast to the expressions found for the IR spectrum, those for the Raman spectrum are more complicated because the intensity also depends on the scattering geometry. When following a static approach, once again, a Taylor expression of the crucial operator term, in this case the polarizability tensor, can be developed in terms of the vibrational eigenstates. For each phonon mode, the corresponding Raman intensity, I_n can be found by applying the properties of harmonic oscillators and the Boltzmann distribution law:

$$I_n(\omega) \sim \frac{\omega_s^4}{\omega(1-e^{-\hbar\omega/k_B T})} \left| \boldsymbol{E}^s\cdot\left(\frac{\partial\alpha}{\partial Q_n}\right)_0\cdot\boldsymbol{E} \right|^2 \delta(\omega_n - \omega) \tag{15}$$

Finally, after determining the isotropic averages in the case of linearly polarized light, the equation is as follows:

$$I_n(\omega) \sim \frac{\omega_s^4}{\omega(1-e^{-\hbar\omega/k_B T})} \left(\frac{45a_n^2 + 7\gamma_n^2}{45}\right) \tag{16}$$

where a_n and γ_n are given by:

$$a_n = \frac{1}{3}\left(\frac{\partial\alpha_{xx}}{\partial Q_n} + \frac{\partial\alpha_{yy}}{\partial Q_n} + \frac{\partial\alpha_{zz}}{\partial Q_n}\right) \tag{17}$$

$$\gamma_n^2 = \frac{1}{2}\left[\left(\frac{\partial\alpha_{xx}}{\partial Q_n} - \frac{\partial\alpha_{yy}}{\partial Q_n}\right)^2 + \left(\frac{\partial\alpha_{yy}}{\partial Q_n} - \frac{\partial\alpha_{zz}}{\partial Q_n}\right)^2 + \left(\frac{\partial\alpha_{zz}}{\partial Q_n} - \frac{\partial\alpha_{xx}}{\partial Q_n}\right)^2\right] + 3\left[\left(\frac{\partial\alpha_{xy}}{\partial Q_n}\right)^2 + \left(\frac{\partial\alpha_{xz}}{\partial Q_n}\right)^2 + \left(\frac{\partial\alpha_{yz}}{\partial Q_n}\right)^2\right] \tag{18}$$

The derivatives of the polarizability tensor with respect to the normal mode coordinate can also be referred to as the components of the Raman tensor, which is a third-order derivative of the energy that can be calculated with linear response or finite difference approaches.[111] Therefore, it requires more computational resources to calculate the Raman tensor compared to the calculation of the BEC.

Similarly as in the dynamic IR case, taking the Fourier transform of the δ function in the expression of the Raman intensity (eq 14) eventually leads to:

https://doi.org/10.1021/acs.jctc.3c00942
J. Chem. Theory Comput. 2024, 20, 513−531

$$I(\omega) \sim \frac{\omega\omega_s^4}{(1-e^{-\hbar\omega/k_BT})}\int dt e^{-i\omega t}\langle(\boldsymbol{E}\cdot\alpha(0)\cdot\boldsymbol{E}^s)(\boldsymbol{E}^s\cdot\alpha(t)\cdot\boldsymbol{E})\rangle_{cl} \tag{19}$$

Analogous to the static case, a general expression for the Raman intensity is obtained by determining the isotropic averages. In the case of linearly polarized light, the expression reduces to:

$$I(\omega) \sim \frac{\omega\omega_s^4}{(1-e^{-\hbar\omega/k_BT})}\left(\frac{45a(\omega)^2+7\gamma(\omega)^2}{45}\right) \tag{20}$$

where $a(\omega)^2$ and $\gamma(\omega)^2$ are given by:

$$a(\omega)^2 = \frac{1}{9}\int dt e^{-i\omega t}\langle(\alpha_{xx}(0)+\alpha_{yy}(0)+\alpha_{zz}(0))(\alpha_{xx}(t)+\alpha_{yy}(t)+\alpha_{zz}(t))\rangle_{cl} \tag{21}$$

$$\begin{aligned}\gamma(\omega)^2 = {} & \frac{1}{2}\int dt e^{-i\omega t}\langle(\alpha_{xx}(0)-\alpha_{yy}(0))(\alpha_{xx}(t)-\alpha_{yy}(t))\rangle_{cl} \\ & + \frac{1}{2}\int dt e^{-i\omega t}\langle(\alpha_{yy}(0)-\alpha_{zz}(0))(\alpha_{yy}(t)-\alpha_{zz}(t))\rangle_{cl} \\ & + \frac{1}{2}\int dt e^{-i\omega t}\langle(\alpha_{zz}(0)-\alpha_{xx}(0))(\alpha_{zz}(t)-\alpha_{xx}(t))\rangle_{cl} \\ & + 3\int dt e^{-i\omega t}\langle\alpha_{xy}(0)\alpha_{xy}(t)\rangle_{cl} + 3\int dt e^{-i\omega t}\langle\alpha_{yz}(0)\alpha_{yz}(t)\rangle_{cl} \\ & + 3\int dt e^{-i\omega t}\langle\alpha_{zx}(0)\alpha_{zx}(t)\rangle_{cl}\end{aligned} \tag{22}$$

Consequently, only the components of the polarizability tensor are required at subsequent time steps to predict the Raman spectrum via MD. The polarizability tensor can be obtained from first-principles calculations via linear response techniques,[112,113] which can increase the computational cost per MD step by one or more orders of magnitude. Therefore, an approximate finite difference scheme is often used, which requires the calculation of the dipole moment with and without applied electric field.[54]

Thermal and Mechanical Properties. The temperature dependent free energy of a material can be expressed in terms of its phonon frequencies:

$$F(T) = E_{el} + \sum_n \frac{\hbar\omega_n}{2} + k_BT\ln(1-e^{-\hbar\omega_n/k_BT}) \tag{23}$$

in which E_{el} is the electronic energy. In the quasi-harmonic approximation (QHA), the vibrational frequencies have an explicit volume dependence. This allows the calculation of thermal and mechanical properties such as the bulk modulus K, the thermal expansion coefficient β_V, and the heat capacities at constant volume, C_V, and constant pressure, C_P, at the equilibrium configuration with volume V_{eq} (see also section S1.3 in the Supporting Information for more details):

$$K(T) = V\frac{\partial^2F(V,T)}{\partial V^2}\bigg|_{V=V_{eq}} \tag{24}$$

$$\beta_V(T) = \frac{1}{V(T)}\frac{\partial V(T)}{\partial T}\bigg|_{V=V_{eq}} \tag{25}$$

$$C_V(T) = -T\frac{\partial^2F(V,T)}{\partial T^2}\bigg|_{V=V_{eq}} \tag{26}$$

$$C_P(T) = C_V(T) + \beta_V^2(T)K(T)V_{eq}(T)T \tag{27}$$

Computational Details. All calculations have been performed with DFT at the PBE-D3(BJ) level of theory.[114−116] The applied software depended on the followed approach. In the static approach, simulations with a plane-wave basis set are performed using the Vienna *Ab Initio* Simulation Package (VASP).[117−119] This particular basis set allows one to easily take into account the periodic nature of the nanostructured materials. However, the large computational cost makes it less suitable for MD simulations. Therefore, the dynamic simulations were executed with CP2K,[105] also using an atomic basis set, which is developed to perform highly efficient MD simulations.

Starting Structures. The starting structures used in this study were mostly obtained from our previous work. The defective-free structures of MIL-53(Al), UiO-66, and $CsPbBr_3$ were taken from, respectively, refs 20, 120, and 63. The UiO-66 structure containing a linker defect is generated by simply removing one linker. The UiO-66 structure containing a cluster defect was generated from the defective-free structure by simply removing one metal cluster together with the linkers attached to it. The connection points of the removed linkers on the remaining metal clusters were capped by a formate group. The starting structure of H-SSZ-13 was generated from the chabazite structure in the database of the International Zeolite Association by introducing two Brønsted acid sites, consisting of an aluminum substitution and an additional proton, in its unit cell. The first acid site could be chosen freely without consequences on the properties due to the symmetry of the system. The second acid site was positioned on a different double six-membered ring more than two silicon positions away to minimize the possible interactions between the acid sites.

Static Approach. Static DFT calculations have been conducted with VASP applying the projector-augmented wave (PAW) method[121] with a plane wave cutoff of 600 eV, an "accurate" precision, and a self-consistent field (SCF) cycle convergence threshold on the electronic energy of 10^{-8} eV. For each structure, a different Monkhorst−Pack k-mesh has been employed.[122] The following k-meshes were used: $6\times2\times2$ for MIL-53(Al) (lp phase), $6\times2\times6$ for MIL-53(Al) (cp phase), $1\times1\times1$ for UiO-66, $4\times4\times3$ for $CsPbBr_3$, and $1\times1\times1$ for H-SSZ-13.

To determine the optimal geometry, a set of fixed volume optimizations around the expected equilibrium volume were performed until the electronic energy did not deviate by more than 10^{-7} eV. Afterward, the corresponding energies were fitted through a Rose−Vinet fit to determine the optimal volume.[123] A final fixed volume optimization was executed at this optimal volume. The Hessian of the equilibrium structure was calculated via finite differences of the forces with respect to the atomic displacements.

The experimental Raman spectra were collected with a maximum photon wavenumber of 25×10^3 cm^{-1} (wavelengths greater than 400 nm), multiple orders of magnitude smaller than the Brillouin zone dimensions of the materials in this study. For all case studies in this contribution, the magnitude of the unit cell vectors is between 10 and 30 Å, corresponding to Brillouin zone dimensions larger than 10^7 cm^{-1} (π/a, with a being the length of an arbitrary unit cell vector). The wavenumbers of the phonons (*i.e.*, the wavenumber difference between the incident and scattered photons) will at most be

https://doi.org/10.1021/acs.jctc.3c00942
J. Chem. Theory Comput. 2024, 20, 513−531

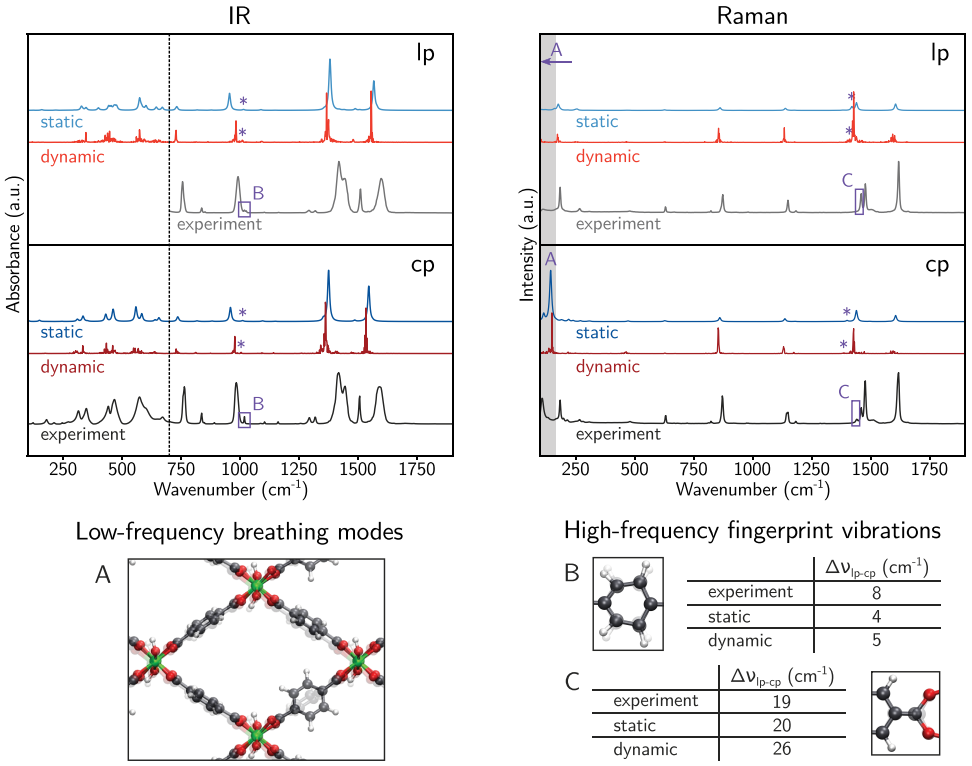

Figure 3. Theoretical and experimental IR and Raman spectra of MIL-53(Al) in the range 100−1900 cm^{-1}. The experimental spectra were measured at room temperature, except for the IR spectrum of the lp phase, which was measured at 413 K. The dynamic spectra were calculated in the NVT ensemble at 300 K. Characteristic fingerprint vibrations are highlighted in the spectrum and visualized: (A) Raman -active linker rotation mode, (B) IR-active bending within the aromatic group and rocking of hydrogen atoms, and (C) Raman-active symmetric stretch within the carboxyl group. The experimental IR and Raman spectra were taken from ref 20. Copyright 2018 American Society. The experimental IR spectrum of the lp phase in the range 100−700 cm^{-1} could not be measured.

the same order of magnitude of the wavenumbers of the incident photons, often much smaller. Similarly, the wavenumbers of the absorbed photons in IR spectroscopy are also much lower than the Brillouin zone dimensions (wavenumber <4000 cm^{-1}, wavelength >2500 nm). Therefore, the experimental spectra will only sample the immediate vicinity of the Brillouin zone-center, and it suffices to only consider the Γ-point phonon modes when computing IR and Raman spectra. The phonon modes in the Γ-point were obtained through a normal-mode analysis. Infrared intensities of these phonon modes were obtained according to the procedure outlined in ref 20. Raman intensities were determined following a procedure already reported in our earlier work,[21] except for UiO-66, whose unit cell was too large and for which a different procedure was adopted (see section S3 in the Supporting Information).

Dynamic Approach. *Ab initio* molecular dynamics simulations have been performed with the CP2K code and its coupled Quickstep module applying a Gaussian and plane wave basis set[124] with 1000 Ry as the plane wave cutoff, 60 Ry as the relative cutoff, a TZVP MOLOPT basis set[125] as the atomic basis set, and GTH pseudopotentials.[126] All MD simulations have been executed in the NVT ensemble starting from the statically optimized structure. The MD simulations have been performed at 300 K, except for the simulations on H-SSZ-13 with and without methanol molecules, which have been run on 373 K. For $CsPbBr_3$, additional NVT simulations on different temperatures have been performed. The cp phase and lp phases of MIL-53(Al) are simulated in a 2 × 1 × 2 supercell, $CsPbBr_3$ is simulated in a 3 × 3 × 2 supercell, and UiO-66 and H-SSZ-13 are simulated in the unit cell (see also section S4 in the Supporting Information). MD trajectories with 50 000 steps have been constructed. A time step of 0.5 fs was chosen for all structures, except for $CsPbBr_3$, for which a time step of 2 fs has been used. The first 10 000 steps served as equilibration and were not considered for the construction of the spectra. The temperature was controlled using a chain of five Nosé−Hoover thermostats with a timeconstant of 100 fs.[103] The dipole moments and polarizability tensors to construct the dynamic IR and Raman spectra, respectively, were calculated every fourth (fifth for $CsPbBr_3$) MD step to reduce the computational load. The latter was determined via a finite difference scheme based on the difference between the dipole moments with and without electric field.[54]

VIBRATIONAL PROPERTIES OF NANOSTRUCTURED MATERIALS

Having introduced the theoretical foundations on how to calculate the various vibrational spectra for nanostructured materials, we will here apply these concepts on the four case studies introduced earlier in this paper. By meticulously comparing theoretical and experimentally derived spectra for the various cases with specific features, *i.e.*, anharmonic behavior, presence of defects, flexible versus rigid behavior, and the presence of guest molecules, a general assessment will be given on which technique is suited for the calculation of vibrational spectra and properties. The experimental spectra are taken from literature or have been measured within the framework of this study, as will be indicated below. We refer to

https://doi.org/10.1021/acs.jctc.3c00942
J. Chem. Theory Comput. 2024, 20, 513−531

section S2 in the Supporting Information for more details on the experimental methodology.

Flexible MIL-53 Materials. Phonon modes govern the lattice dynamics within crystals. In that sense, they are directly involved in the flexibility of functional materials.[41,127] MIL-53(Al) is the prototype of a flexible MOF consisting of 1D aluminum-oxide chains connected by benzenedicarboxylate (BDC) linkers forming a wine-rack topology.[60] A change in thermodynamic conditions (such as temperature, pressure, or guest adsorption) can trigger a breathing transition between a closed pore (cp) and a large pore (lp) phase.[128−130] The occurrence of this phase transition depends on a detailed balance between dispersion interactions and vibrational entropy.[33,34] The latter is primarily dominated by contributions due to low-frequency phonon modes. As these terahertz vibrations heavily depend on dispersion interactions, their vibrational frequencies can differ substantially depending on the phase the material is in. Consequently, the terahertz region is characteristic for each phase and the respective phonon modes play a crucial role in the phase transition mechanism.[20,131] To accurately model flexibility in MIL-53(Al), it is therefore required that the low-frequency phonon modes are predicted correctly.

In Figure 3, the static and dynamic IR and Raman spectra of both the cp and lp phases of MIL-53(Al) in the range 100−1900 cm^{-1} are compared with the experimental spectra reported in ref 20. It needs to be clarified that no literature data were available for the experimental IR spectrum of the lp phase in the frequency range 100−700 cm^{-1} due to limitations on imposing the required *in situ* conditions.[20] Furthermore, the experimental Raman spectrum of the so-called cp phase is actually the Raman spectrum of a mixture of structures in the cp and lp phases as a result of sample heating due to the Raman laser.[20] A first observation is that the static and dynamic spectra are nearly identical, which suggests that the IR- and Raman-active phonon modes in these crystalline porous structures behave almost harmonically. Additionally, a very good correspondence can be noted between theory and experiment. This is particularly important in the low-frequency region depending on weak interactions, which are hard to model correctly. On the lower edge of the measured frequency range, an intense Raman band is observed in the cp phase (mode A in Figure 3), which is assigned to phonon modes inducing linker rotations.[21] The theoretical Raman band is slightly blue-shifted with respect to the experiment, which originates from a difference in unit cell volume between the theoretical cp phase structure and the experimentally measured one.[131] The sound agreement between theory and experiment allows even prediction of a shift from the phonon mode inducing linker rotations to lower frequencies when going from the cp to the lp phase. As this band is located below 100 cm^{-1} in the lp phase, it could not be measured due to optical limitations of the experimental setup.[20] Nevertheless, a Raman study on topologically similar structures indicated this band should indeed be present.[21] An important consideration regarding the accurate prediction of the low-frequency vibrational spectrum is the system size. When the unit cell is too small to correctly account for long-range interactions, a sufficiently large *k*-point mesh or supercell should be applied. Otherwise the prediction of the low-frequency spectrum will be wrong, which is illustrated in section S4 of the Supporting Information.

It is clear that both static and dynamic approaches reliably describe the significant differences in the low-frequency spectra of the MIL-53(Al) phases. Moreover, they can also predict more subtle shifts between the cp and lp phase phonon modes in the higher frequency range. This can be of interest when one has no access to sophisticated terahertz equipment and wants to distinguish the lp phase spectrum from the cp phase spectrum. In the IR spectrum, the characteristic phonon mode due to bending within the aromatic group and rocking of hydrogen atoms (mode B in Figure 3) exhibits an experimental shift of 8 cm^{-1} when going from the cp phase to the lp phase.[132] This blue-shift is reproduced by the two theoretical approaches. In the Raman spectrum, the characteristic symmetric stretching mode within the carboxyl group (mode C in Figure 3) shows an even larger shift of 19 cm^{-1} when going from the cp to the lp phase,[133] which is again correctly predicted by the static and dynamic simulations.

Besides the direct spectroscopic comparison between theory and experiment, the accuracy of the theoretical phonon modes can also be estimated by their ability to predict mechanical and thermal properties. The first row of Table 1 compares the bulk modulus, the volumetric thermal expansion, and the specific heat capacity at constant pressure of the lp phase calculated via QHA with experimental reference values at 300 K. The bulk modulus of the lp phase of MIL-53(Al) has a very low theoretical value of 3.3 GPa, indicating that the structure is indeed very flexible, although it is still one order of magnitude higher than the experimental reference value.[129] These theoretical results compare well with theoretical bulk moduli from other researchers. We refer to section S7 in the Supporting Information for a detailed comparison with literature. Nevertheless, this deviation is mainly caused by the contribution of the electronic energy to the free energy. The calculated volumetric thermal expansion coefficient and specific heat capacity at constant pressure are slightly overestimated with respect to the experiment. The higher theoretical value of the specific heat capacity indicates that, in general, the calculated vibrational frequencies of the low-frequency phonon modes are underestimated. As low-frequency modes contribute more strongly to the thermal expansion and because these modes predominantly contribute to positive thermal expansion,[131] this also leads to a higher value of the thermal expansion coefficient.

Table 1. Bulk Modulus *K*, Volumetric Thermal Expansion α_V, and Heat Capacity at Constant Pressure C_p of the Four Different Functional Materials Considered in This Review[a]

	K(GPa)		α_V (10^{-6} K^{-1})		C_p (J g^{-1} K^{-1})	
	QHA	exp	QHA	exp	QHA	exp
MIL-53(Al) (lp phase)	3.3	0.4[129]	71	19[128]	0.98	0.86[134]
UiO-66	49	17[135]	−2	−17[136]	0.78	0.78[137]
$CsPbBr_3$	16	16[138]	103	114[139]	0.19	0.19[140]
H-SSZ-13	53		−16	−24[141]	0.76	

[a]Theoretical values were derived via QHA at 100 K for $CsPbBr_3$ and at 300 K for the other structures. Experimental reference values were found in the literature.

In summary, both static and dynamic approaches are able to correctly predict vibrational properties of the flexible MOF MIL-53(Al) provided that sufficiently large supercells or *k*-

https://doi.org/10.1021/acs.jctc.3c00942
J. Chem. Theory Comput. 2024, 20, 513−531

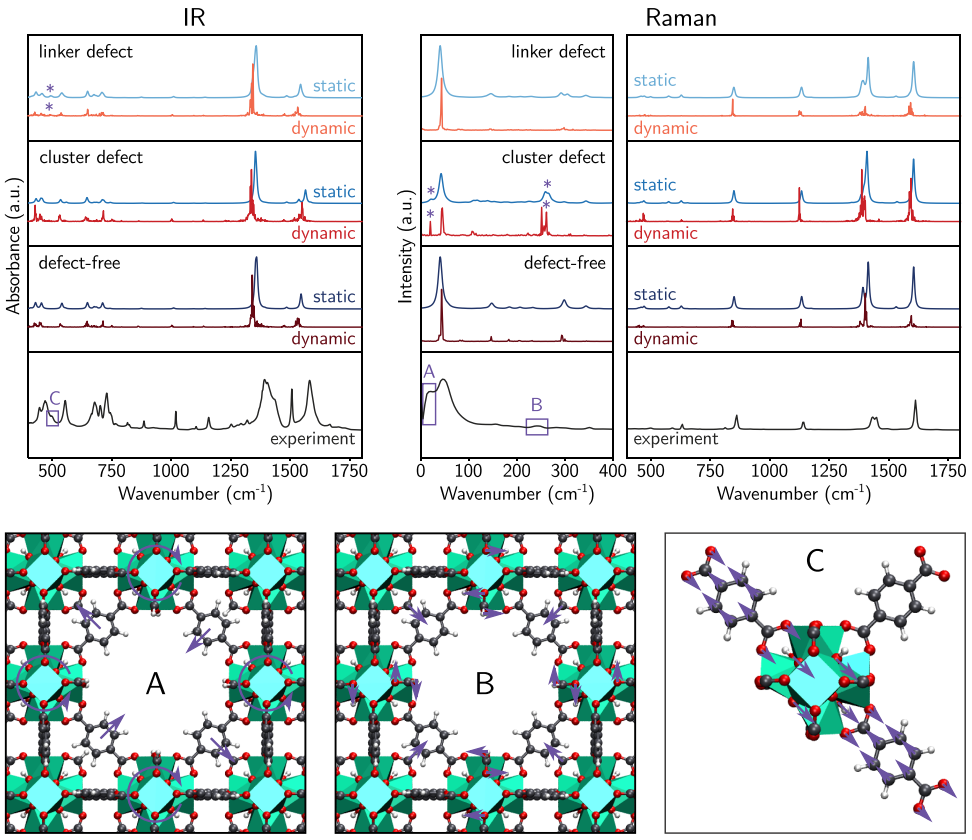

Figure 4. Theoretical and experimental IR (400−1800 cm^{-1}) and Raman spectra (0−1800 cm^{-1}) of UiO-66. The experimental spectra were recorded at room temperature. The dynamic spectra were calculated in the NVT ensemble at 300 K. Characteristic fingerprint vibrations are highlighted in the spectrum and visualized: (A) Raman-active rotation of the metal node and translation of the linker, (B) Raman-active rocking of the formate group, and (C) IR-active rocking of the hydroxyl group. The experimental IR spectrum was taken from ref 149. Copyright 2014 American Chemical Society.

meshes are considered to account for the long-range interactions.

Point Defects in UiO-66. All crystalline materials are, to a certain extent, subject to defects. They can be an unwanted source of instability, but they can just as well be engineered to tune the material properties toward specific applications.[142,143] Within the field of MOFs, the concept of defect engineering is well established and used as a design parameter.[142] In this regard, an important aspect is the interaction between phonons and defects leading to a change in the phonon spectrum and its corresponding properties.[144] Theory is often required to characterize these defect−phonon interactions given the limited spatial resolution of most experimental techniques.[144] Here, the ability of static and dynamic theoretical approaches to capture the effect of two types of point defects on phonon properties will be assessed through the study of UiO-66, a MOF containing Zr oxide clusters as metal nodes connected by BDC linkers.[61] The 12-fold linker connectivity of each metal-oxide cluster renders this material very stable,[145] allowing for the introduction of defects without destroying the structure.[146] The combination of two different building blocks immediately gives rise to two types of point defects: a missing linker defect[147] and a missing cluster defect.[148]

In Figure 4, the theoretical IR and Raman spectra of UiO-66 structures containing these types of defects are reported. They are compared with the theoretical spectra of defect-free UiO-66 and with the experimental spectra of samples of UiO-66 including an, *a priori*, unknown set of defects. The experimental IR spectra have already been reported in the work of Chavan et al.,[149] but these are restricted to the mid-IR region. The measurement of the far-IR region often requires a different optical setup making this part of the IR spectrum more difficult to obtain.[20] However, the low-frequency spectrum could be studied through original Raman spectra, which were measured for the purpose of this study. As was the case for MIL-53(Al), the static and dynamic approaches yield very similar spectra. This is especially so for wavenumbers above 100 cm^{-1}. However, at lower wavenumbers the Raman spectrum of UiO-66 containing a cluster defect has one band, around 20 cm^{-1}, with significantly deviating intensity between the two approaches. The presence of a cluster defect decreases the connectivity of the framework, softening the material and leading to a flatter PES. Consequently, the minimum of the PES is less easily described by a harmonic potential. The low-frequency modes, in particular, will be more prone to anharmonic behavior. As the presence of defects can primarily be observed through fingerprints in the low-frequency spectrum,[43,150] the simulation of the corresponding phonon modes benefits from the dynamic approach. The experimental Raman spectrum of our UiO-66 sample does indeed feature a Raman band at 20 cm^{-1} (mode A in Figure 4), which can, with the help of our simulations, be assigned to the presence of a cluster defect. Apparently, the removal of a metal-oxide cluster renders the phonon mode inducing rotations of the remaining metal-oxides and translations of the organic linkers Raman-active.

https://doi.org/10.1021/acs.jctc.3c00942
J. Chem. Theory Comput. 2024, 20, 513−531

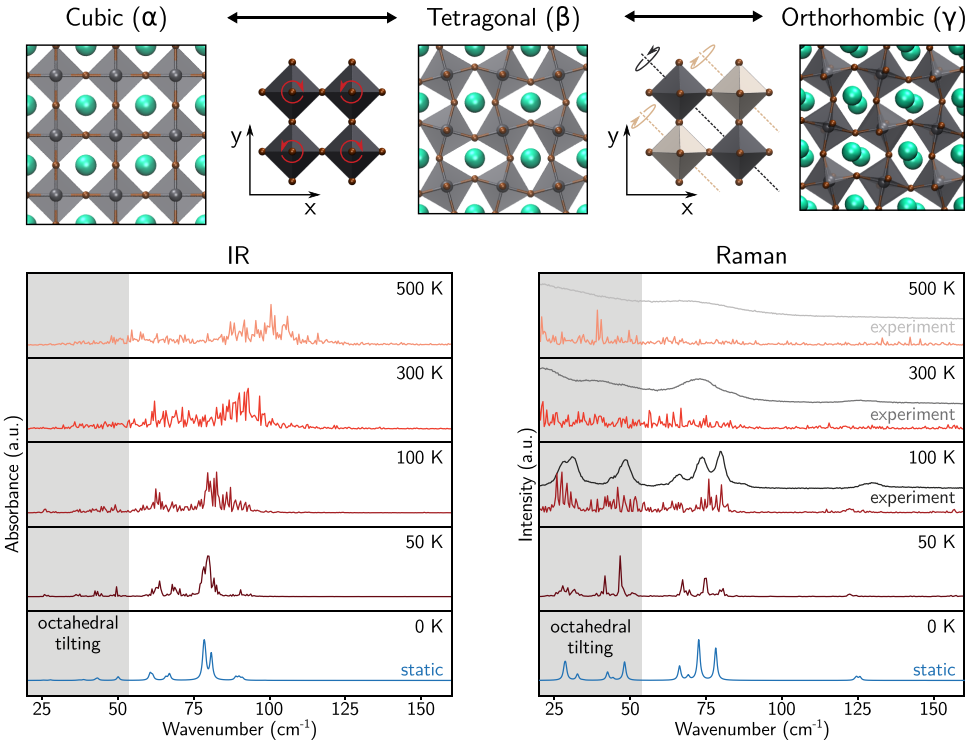

Figure 5. (Top) The three phases of $CsPbBr_3$ with schematic illustration of the tilting mechanisms inducing phase transitions. (Bottom) Theoretical IR and Raman spectra of the γ-phase in the range 20−160 cm^{-1} at different temperatures. Experimental Raman spectra (gray) were measured at 100, 300, and 500 K. The red spectra are obtained via AIMD, and the blue spectra are the result of a static calculation (0 K). The frequency region containing the phonon modes inducing octahedral tilting is indicated. The theoretical and experimental Raman spectra were already presented in ref 63 distributed under a Creative Commons Attribution (CC BY) license. Copyright 2023 The Authors.

The existence of this low-frequency Raman band in the experimental spectrum clearly confirms the presence of cluster defects in the sample. Nevertheless, less pronounced vibrational fingerprints of defects pop up at higher frequencies, which are also predicted by theory irrespective of the followed approach. The experimental Raman spectrum exhibits a weak Raman-active band around 240 cm^{-1} (mode B in Figure 4), which again indicates that cluster defects have been formed. This mode originates from the formate groups that cap the metal clusters that should otherwise be connected with the missing cluster. Furthermore, the theoretical Raman spectra of UiO-66 featuring cluster defects predict an altered band shape for the modes inducing symmetric stretching of the carboxyl group around 1430 cm^{-1}. However, as these bands overlap with those of the defect-free structure, it is difficult to isolate this deviation in the experimental spectrum.[151] Interestingly, the Raman spectrum of the UiO-66 structure including a missing linker defect closely resembles the one of the defect-free UiO-66. Consequently, the missing linker defect has no obvious Raman-active fingerprint vibration. In contrast, its IR spectrum provides a characteristic phonon mode around 500 cm^{-1}, which is not present in the case of a defect-free structure or with a missing cluster defect (mode C in Figure 4). This phonon mode induces mainly rocking of the hydroxyl groups on the metal-oxide cluster. The experimental IR spectrum, which was reported by Chavan et al.,[149] features a weakly IR-active band at this frequency, indicating that the sample is affected by such linker defects. The IR spectrum of UiO-66 with a missing cluster defect shows no clear fingerprint vibrations except for the antisymmetric stretching vibrations of the carboxyl group around 1580 cm^{-1}, which splits in two contributions. As these contributions overlap with the IR band of the defect-free structure, the presence of missing cluster defects in the experimental sample can be deduced from a broad IR band at the respective frequency range.

Not only the IR and Raman spectra can be reliably predicted by theory but also the mechanical and thermal properties obtained via QHA on the defect-free UiO-66 structure match closely with experimental literature references at 300 K (see Table 1). Although the theoretical bulk modulus is slightly overestimated by theory, probably because of defects in the experimental sample softening the material, it is predicted to be significantly more rigid than that of MIL-53(Al), in agreement with experiment.[135] Furthermore, the volumetric thermal expansion coefficient is correctly predicted to be slightly negative.[136] The property with the largest dependency on the phonon modes, *i.e.*, the specific heat capacity, even matches exactly with the experimental reference value.[137]

From the above case study, it can be concluded that dynamic simulation techniques more reliably predict vibrational fingerprints of defects in MOFs than static ones. This is especially true in the low-frequency region, which is more prone to anharmonic behavior.

Anharmonicity in Metal−Halide Perovskites. Anharmonic behavior forms a great challenge for the accurate prediction of phonon properties. It is completely ignored in the static approach if only harmonic force constants are considered, and the dynamic approach is also not able to fully account for anharmonicities, since it neglects mode coupling and Fermi resonances.[54] Therefore, it is worthwhile to investigate the capacity and limitations of static and dynamic approaches in predicting phonon properties of highly

https://doi.org/10.1021/acs.jctc.3c00942
J. Chem. Theory Comput. 2024, 20, 513−531

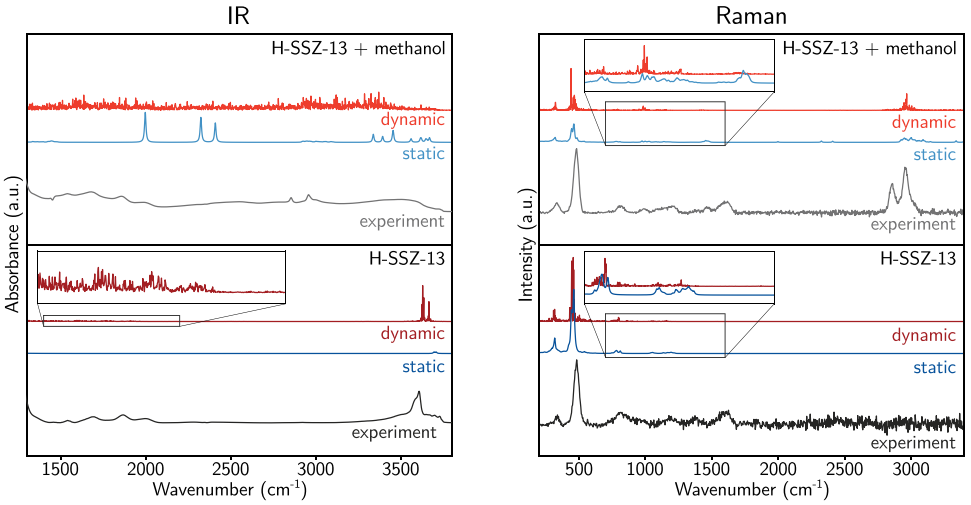

Figure 6. Theoretical and experimental IR and Raman spectra of H-SSZ-13 with and without methanol. The IR spectra are presented in the range 1300−3800 cm^{-1}, and the Raman spectra are presented in the range 200−3400 cm^{-1}. The experimental spectra and the dynamic spectra in the NVT ensemble were obtained at 373 K. The intensities of the dynamic IR spectra were increased with a factor of 5 compared to the static simulation.

anharmonic systems. For that purpose, the phonon spectrum of the all-inorganic MHP $CsPbBr_3$ will be determined. Macroscopically, $CsPbBr_3$ is observed in three different phases: the cubic α-phase, the tetragonal β-phase, and the orthorhombic γ-phase.[62] The three phases can transition from one phase to the other via specific phonon modes inducing tilting of the $PbBr_6$ octahedra (see Figure 5). These phonon modes are anharmonic in the sense that they describe a double-well potential.[152,153] This makes the α- and β-phases unstable at low temperatures. Recent reports even show that, at high temperatures, these phases only appear as averages over long length and time scales, while microscopically the γ-phase is observed.[154−156] Because the octahedral tilting has a strong impact on the electronic properties such as the band gap,[157] it directly affects its efficiency for their usage in optical applications such as solar cells.[22] To gain insight in the dynamics of this octahedral tilting via theory, it is therefore required that the corresponding phonon modes are correctly sampled.

Figure 5 presents the theoretical IR and Raman spectra of the γ-phase of $CsPbBr_3$ at different temperatures obtained with dynamic simulation methods. The Raman spectra have already been presented in ref 63, whereas the IR spectra have been calculated for the purpose of this work. The static spectra, corresponding with the situation at 0 K, are very similar to the dynamic spectra at 50 K. This indicates that at very low temperatures the lattice dynamics in $CsPbBr_3$ behaves nearly harmonically. The phonon modes inducing octahedral tilting are found below 50 cm^{-1}, some of them yielding pronounced Raman bands. At higher wavenumbers, phonon modes typically induce distortions of the octahedra. These distortions can be IR- and/or Raman-active. At 100 K, the optically active bands found at lower temperatures start to broaden due to anharmonic effects. Nevertheless, the different bands can still be recognized. Looking at the experimental Raman spectrum at 100 K, already reported in ref 63, some broad Raman peaks can be identified that match closely with the theoretical prediction. Consequently, the limited level of anharmonicity is well predicted by theory at this temperature. By increasing the temperature, the bands in the theoretical IR and Raman spectra continue to broaden. At 300 and 500 K, it is no longer possible to identify separate optically active bands. In the IR spectrum, there is strong IR activity at wavenumbers above 75 cm^{-1}. Furthermore, this IR activity is observed at higher frequencies than at lower temperatures. This increase in vibrational frequency is in agreement with literature reports.[158] The theoretical Raman spectrum is characterized by a lot of noise and has a monotonously increasing intensity toward 0 cm^{-1}. The noise could be reduced by averaging over several long AIMD runs; however, given the computational cost, this was not feasible. This central peak originates from local polar thermal fluctuations according to Yaffe et al.[155] This monotonously increasing shape is in correspondence with experimental spectra at these temperatures. However, the noise on the theoretical spectrum hinders the identification of additional Raman bands that are superposed to the central line shape in the experimental spectrum. In spite of this, it is clear that anharmonic effects should definitely be taken into account to gain insight in the phonon modes at high temperatures, as the harmonically predicted spectra completely fail in reproducing the experiment.

Analysis of the QHA-derived properties at 100 K indicate an almost exact agreement with reference values from literature (see Table 1). Only the predicted volumetric thermal expansion is slightly underestimated with respect to experiment. This designates that, despite the onset of anharmonicity at this temperature, the harmonic approximation is still capable of reliably capturing phonon properties.

In conclusion, the case of $CsPbBr_3$ showed that the vibrational properties of a highly anharmonic system should, in principle, be calculated following a dynamic approach. However, for sufficiently low temperatures the anharmonic behavior may still be suppressed and a static approach can already yield a correct prediction of the vibrational spectrum.

Guest Species in H-SSZ-13. The previous three case studies focused on the framework phonon modes of both porous and nonporous materials. In many applications of nanoporous frameworks, such as catalysis or adsorption, the voids of these crystals are occupied by guest species. The interaction between these molecules and the framework can

https://doi.org/10.1021/acs.jctc.3c00942
J. Chem. Theory Comput. 2024, 20, 513−531

lead to changes in the vibrational spectra of both.[47] Therefore, we also consider the case of the acidic zeolite H-SSZ-13 that is loaded with methanol molecules. This application is inspired by the methanol-to-olefin process.[159−161] H-SSZ-13 is a popular heterogeneous catalyst for the conversion of molecules like methanol to other chemical building blocks like ethene and propene.[4] Such catalytic processes often involve a vast number of reaction intermediates making it very difficult to follow the reaction under *operando* conditions. As each of these intermediates feature unique vibrational fingerprints the reaction mechanism can, in principle, be fully characterized by analyzing the evolution of the vibrational spectra in the course of the reaction. This is true provided that the experimental setup allows to measure under *operando* conditions. Such approach was followed in the work of Lezcano-Gonzalez et al. to track the conversion of methanol under *operando* conditions making use of Kerr-gated Raman spectroscopy.[44] In practice, however, some bands of the reaction intermediates will overlap, hindering their identification. Therefore, theory is quintessential to assign the different spectral contributions.[44,48] In that regard, the accurate sampling of host−guest interactions is important to correctly predict the vibrational spectra. The study of inorganic zeolites in contrast to inorganic−organic frameworks like MOFs is particularly beneficial to assess the impact of host−guest interactions on the vibrational fingerprints because the inorganic framework modes exhibit primarily low wavenumbers that have little overlap with the vibrational frequencies of the organic guest species.

The theoretical and experimental IR and Raman spectra of H-SSZ-13 with and without methanol are presented in Figure 6. Both experimental and theoretical spectra were generated for the purpose of this Review. The experimental IR spectra are only available for wavenumbers above 1300 cm^{-1} because of optical limitations. The theoretical IR spectra below 1300 cm^{-1} are presented in Figure S18 in the Supporting Information. The vibrational spectra can be subdivided in two parts. For wavenumbers below 1200 cm^{-1}, mainly framework modes can be identified. Their spectra are almost identical for the static and dynamic approaches, as was already observed for the framework modes of MIL-53(Al) and UiO-66. The theoretical Raman spectra in this range also match well with experiment. Furthermore, the impact of guest species on the framework modes fingerprints is limited to some small intensity changes. Therefore, the harmonic approximation is perfectly capable of predicting the phonon modes of the host framework. Above 1200 cm^{-1}, H-SSZ-13 without guests features no framework modes except for the OH-wagging and OH-stretch vibrations assigned to the Brønsted acid sites. The theoretical spectra partially predict these bands; however, the experimental spectra also feature bands due to silanol groups, which are not incorporated in our model. Interestingly, the dynamic simulation correctly predicts IR-active OH-wagging modes between 1400 and 2000 cm^{-1}, in agreement with the experiment. However, no phonon modes were found in this range in the static simulation. The modes due to acid sites largely disappear upon interaction with the methanol guests. Consequently, the high frequency region contains primarily fingerprints of methanol in the case of the guest-loaded sample.

The quality of the predicted guest spectra differs for the IR and the Raman spectra. In the case of IR spectra, the static approach yields clear IR-active bands due to the methanol molecules. These bands do not correspond with the experimentally observed bands. Clearly the case of highly mobile and interacting guest molecules can not be simulated through a simple harmonic approximation. However, the dynamic approach is also not very well suited to predict the IR spectrum, as it gives rise to a very weak and noisy spectrum. This probably stems from interactions between the methanol molecules, which are subject to strong hydrogen bonds and are primarily IR-active. Complete sampling of these interactions requires a much longer simulation time. Less reactive guest molecules such as ethylene do not suffer from this issue. Consequently, the dynamically predicted IR spectrum more closely resembles the experiment, as seen in Figures S19 and S20 in the Supporting Information.

The problem encountered in the dynamic IR spectra is less pronounced for the Raman spectra because Raman activity does not strongly depend on hydrogen bonding interactions. The Raman fingerprints of the guests can be observed in both the static and dynamic approaches. It becomes immediately clear that the static Raman spectra of the guest species yield more Raman-active bands than the dynamic spectra. This is a consequence of the single configuration that is considered in the static case. However, as the PES of a host−guest system is very flat, a large variety of configurations can be reached in reality. The Raman-active bands strongly depend on the particular configuration. Hence, Raman bands that pop up in one configuration can be totally absent in another configuration. Dynamic sampling of the PES averages out all contributions and yields a more reliable vibrational spectrum of the guest species. This is confirmed by the comparison of the experimental and theoretical spectra for which the dynamic approach yields a better correspondence. Another advantage of dynamic over static simulations is a better sampling of the interaction of the guest molecules with the Brønsted acid sites. Consequently, methanol molecules become protonated within zeolites during MD simulations, which is also experimentally observed.[162] The protonation removes the Brønsted acid sites and the corresponding Raman band in the dynamic spectrum. In contrast, the static Raman spectrum is still characterized by bands due to the acid sites.

Finally, the QHA-derived thermal and mechanical properties of the empty H-SSZ-13 framework are considered at 300 K. As this zeolite is mainly used for catalytic application, its experimental characterization with respect to these type of properties is limited. Therefore, no reference values of the bulk modulus and the specific heat capacity are available. Although the volumetric heat capacity has been measured,[141] it yields a substantial negative value, in correspondence with the QHA simulation, indicating that our model correctly predicts the negative thermal expansion characteristic for many zeolites.[163]

The case of methanol in H-SSZ-13 zeolite indicates that a dynamic approach is required to calculate the vibrational fingerprints of guest species in order to correctly sample the multitude of configurations these species can adopt in the host system.

CONCLUSIONS AND THEORETICAL GUIDELINES FOR CALCULATING VIBRATIONAL SPECTRA IN NANOSTRUCTURED MATERIALS

Thorough characterization of functional nanostructured materials is important in order to improve their performance. In that regard, vibrational spectroscopy is well suited, as it allows the study of both their structural and dynamical features. For the interpretation of the resulting vibrational

https://doi.org/10.1021/acs.jctc.3c00942
J. Chem. Theory Comput. 2024, 20, 513−531

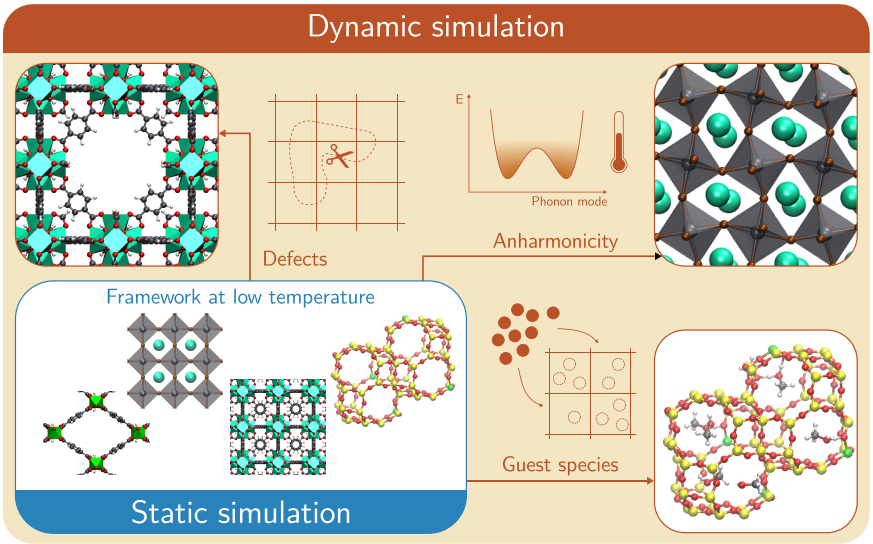

Figure 7. Schematic visualization of the guidelines to accurately predict vibrational properties.

spectra, theoretical simulations are of primary importance. To this end, it is vital to know which simulation techniques are reliable to derive the vibrational properties of realistic nanostructured materials with and without pores, defects, and guest molecules. On the one hand, the vibrational spectrum can be determined through a static approach where the PES is approximated by a set of harmonic oscillators in its equilibrium configuration at 0 K. On the other hand, within a dynamic approach, a range of configurations is sampled around the equilibrium configuration, following the system in time by integrating Newton's equations of motion. Consequently, anharmonicity in the PES and temperature effects are inherently accounted for in the dynamic approach. Notwithstanding the proven success of both theoretical approaches in unraveling phonon properties in functional nanostructured materials, a thorough analysis of which method to use under specific circumstances is lacking.

In this Review, the ability of the static and dynamic approaches to accurately predict phonon properties in functional nanostructured materials has been assessed by means of four different case studies, each focusing on a specific material's aspect. These case studies clearly illustrate the possibilities and limitations of both approaches. This allows us to propose guidelines on which method should be employed in a specific situation (see Figure 7). As a general rule, the framework phonon modes follow the harmonic regime at sufficiently low temperatures when the solid-state system contains neither defects nor guest molecules. In that case, the static approach relying on a harmonic approximation of the PES can be applied to characterize the phonon modes and gain insight in the lattice dynamics. For example, statically predicted vibrational spectra of the cp and lp phases of MIL-53(Al) were in close agreement with experiment allowing to interpret the mechanism behind the breathing transition.

With increasing temperature, anharmonic phonon modes can deviate substantially from the harmonic behavior, under those circumstances dynamic sampling may be required. The temperature threshold at which the harmonic regime no longer holds heavily depends on the system. For the perovskite $CsPbBr_3$, this threshold was exceeded between 100 and 300 K, whereas the zeolite and MOFs studied here were still behaving harmonically between 300 and 400 K. Also, when the PES is relatively flat, dynamic sampling is preferred. A first example is the introduction of point defects in the framework such as UiO-66. This will mainly affect low-frequency phonon modes, visible in the terahertz spectrum, influencing the lattice dynamics and their related properties. A second example is the presence of guest molecules in the framework. In contrast to the host framework, these guest molecules experience a high configurational freedom. Therefore, their vibrational spectrum may vary significantly with their position inside the framework and dynamic sampling is required to obtain an averaged picture.

These general guidelines may serve as a starting point to choose an appropriate model for the calculation of phonon properties in nanostructured materials. Nevertheless, other modeling parameters should also be thoroughly considered such as the simulated system size, which needs to be sufficiently large to accurately take into account long-range interactions. This is especially important when the effect of realistic defects on the phonon properties has to be investigated.

■ ASSOCIATED CONTENT

Data Availability Statement

All structure files and input scripts used to obtain the computational results are available from the online GitHub repository at https://github.com/AlexanderHoffman/supporting-info.

Supporting Information

The Supporting Information is available free of charge at https://pubs.acs.org/doi/10.1021/acs.jctc.3c00942.

> Derivation of the theoretical formulas to compute IR and Raman intensities, formulas of thermal and mechanical properties, experimental details, computation of static Raman intensities via numerical second-order derivatives, effect of supercell size, temperature dependence of QHA-derived properties, additional vibrational spectra of H-SSZ-13, and a comparison of bulk moduli from this work with other results from literature (PDF)

https://doi.org/10.1021/acs.jctc.3c00942
J. Chem. Theory Comput. 2024, 20, 513−531

AUTHOR INFORMATION

Corresponding Author

Veronique Van Speybroeck − *Center for Molecular Modeling, Ghent University, 9000 Ghent, Belgium;* orcid.org/0000-0003-2206-178X; Email: Veronique.VanSpeybroeck@UGent.be

Authors

Alexander E. J. Hoffman − *Center for Molecular Modeling, Ghent University, 9000 Ghent, Belgium;* orcid.org/0000-0002-1529-4705

Wim Temmerman − *Center for Molecular Modeling, Ghent University, 9000 Ghent, Belgium*

Emma Campbell − *Cardiff Catalysis Institute, Cardiff University, Cardiff CF10 3AT, United Kingdom; Research Complex at Harwell, Didcot OX11 0FA, United Kingdom*

Alessandro Ali Damin − *Department of Chemistry, University of Turin, 10124 Turin, Italy;* orcid.org/0000-0002-1110-0993

Ines Lezcano-Gonzalez − *Department of Chemistry, University College London, London WC1E 6BT, United Kingdom; Research Complex at Harwell, Didcot OX11 0FA, United Kingdom*

Andrew M. Beale − *Department of Chemistry, University College London, London WC1E 6BT, United Kingdom; Research Complex at Harwell, Didcot OX11 0FA, United Kingdom;* orcid.org/0000-0002-0923-1433

Silvia Bordiga − *Department of Chemistry, University of Turin, 10124 Turin, Italy;* orcid.org/0000-0003-2371-4156

Johan Hofkens − *Department of Chemistry, KU Leuven, 3000 Leuven, Belgium; Max Planck Institute for Polymer Research, 55128 Mainz, Germany;* orcid.org/0000-0002-9101-0567

Complete contact information is available at: https://pubs.acs.org/10.1021/acs.jctc.3c00942

Notes

The authors declare no competing financial interest.

ACKNOWLEDGMENTS

V.V.S. acknowledges the Research Fund of Ghent University (BOF) and the Research Foundation−Flanders (FWO) for their financial support. V.V.S. and J.H. furthermore acknowledge the Research Fund of Ghent University and the KU Leuven Research Fund (iBOF-21-085 PERSIST). A.M.B. and I.L.-G. kindly thank EPSRC for financial support via Grants EP/R026939/1 and EP/K007467/1 and the Central Laser Facility (CLF) for beamtime (reference 22130028). J.H. also thanks the Flemish government through long-term structural funding Methusalem (CASAS2, Meth/15/04). A.D. and S.B. thank the MUR (Department of Excellence 2023-2027, CUP:D13C22003520001, CH4.0 project). The computational resources and services used in this work were provided by the Flemish Supercomputer Center (VSC), funded by the FWO and the Flemish Government.

REFERENCES

(1) Dzhagan, V. M.; Azhniuk, Y. M.; Milekhin, A. G.; Zahn, D. R. T. Vibrational spectroscopy of compound semiconductor nanocrystals. *J. Phys. D: Appl. Phys.* **2018**, *51*, 503001.

(2) Li, J.; Corma, A.; Yu, J. Synthesis of new zeolite structures. *Chem. Soc. Rev.* **2015**, *44*, 7112−7127.

(3) Li, Y.; Yu, J. Emerging applications of zeolites in catalysis, separation and host−guest assembly. *Nat. Rev. Mater.* **2021**, *6*, 1156−1174.

(4) Yarulina, I.; Chowdhury, A. D.; Meirer, F.; Weckhuysen, B. M.; Gascon, J. Recent trends and fundamental insights in the methanol-to-hydrocarbons process. *Nat. Catal.* **2018**, *1*, 398−411.

(5) Song, J.; Wang, Y.; Walter, E. D.; Washton, N. M.; Mei, D.; Kovarik, L.; Engelhard, M. H.; Prodinger, S.; Wang, Y.; Peden, C. H. F.; Gao, F. Toward rational design of Cu/SSZ-13 selective catalytic reduction catalysts: implications from atomic-level understanding of hydrothermal stability. *ACS Catal.* **2017**, *7*, 8214−8227.

(6) Han, L.; Cai, S.; Gao, M.; Hasegawa, J.-y.; Wang, P.; Zhang, J.; Shi, L.; Zhang, D. Selective catalytic reduction of NO_x with NH_3 by using novel catalysts: State of the art and future prospects. *Chem. Rev.* **2019**, *119*, 10916−10976.

(7) Kosinov, N.; Gascon, J.; Kapteijn, F.; Hensen, E. J. M. Recent developments in zeolite membranes for gas separation. *J. Membr. Sci.* **2016**, *499*, 65−79.

(8) Bereciartua, P. J.; Cantín, Á.; Corma, A.; Jordá, J. L.; Palomino, M.; Rey, F.; Valencia, S.; Corcoran, E. W., Jr; Kortunov, P.; Ravikovitch, P. I.; Burton, A.; Yoon, C.; Wang, Y.; Paur, C.; Guzman, J.; Bishop, A. R.; Casty, G. L. Control of zeolite framework flexibility and pore topology for separation of ethane and ethylene. *Science* **2017**, *358*, 1068−1071.

(9) Shamzhy, M.; Opanasenko, M.; Concepción, P.; Martínez, A. New trends in tailoring active sites in zeolite-based catalysts. *Chem. Soc. Rev.* **2019**, *48*, 1095−1149.

(10) Furukawa, H.; Cordova, K. E.; O'Keeffe, M.; Yaghi, O. M. The chemistry and applications of metal-organic frameworks. *Science* **2013**, *341*, 1230444.

(11) Jiao, L.; Seow, J. Y. R.; Skinner, W. S.; Wang, Z. U.; Jiang, H.-L. Metal−organic frameworks: Structures and functional applications. *Mater. Today* **2019**, *27*, 43−68.

(12) Zhang, X.; Chen, Z.; Liu, X.; Hanna, S. L.; Wang, X.; Taheri-Ledari, R.; Maleki, A.; Li, P.; Farha, O. K. A historical overview of the activation and porosity of metal−organic frameworks. *Chem. Soc. Rev.* **2020**, *49*, 7406−7427.

(13) Kalmutzki, M. J.; Hanikel, N.; Yaghi, O. M. Secondary building units as the turning point in the development of the reticular chemistry of MOFs. *Sci. Adv.* **2018**, *4*, No. eaat9180.

(14) Jiao, L.; Wang, Y.; Jiang, H.-L.; Xu, Q. Metal−organic frameworks as platforms for catalytic applications. *Adv. Mater.* **2018**, *30*, 1703663.

(15) Zhao, X.; Wang, Y.; Li, D.-S.; Bu, X.; Feng, P. Metal−organic frameworks for separation. *Adv. Mater.* **2018**, *30*, 1705189.

(16) Lawson, H. D.; Walton, S. P.; Chan, C. Metal−organic frameworks for drug delivery: a design perspective. *ACS Appl. Mater. Interfaces* **2021**, *13*, 7004−7020.

(17) Yi, F.-Y.; Chen, D.; Wu, M.-K.; Han, L.; Jiang, H.-L. Chemical sensors based on metal−organic frameworks. *ChemPlusChem.* **2016**, *81*, 675−690.

(18) Horike, S.; Shimomura, S.; Kitagawa, S. Soft porous crystals. *Nat. Chem.* **2009**, *1*, 695−704.

(19) Schneemann, A.; Bon, V.; Schwedler, I.; Senkovska, I.; Kaskel, S.; Fischer, R. A. Flexible metal−organic frameworks. *Chem. Soc. Rev.* **2014**, *43*, 6062−6096.

(20) Hoffman, A. E. J.; Vanduyfhuys, L.; Nevjestić, I.; Wieme, J.; Rogge, S. M. J.; Depauw, H.; Van Der Voort, P.; Vrielinck, H.; Van Speybroeck, V. Elucidating the vibrational fingerprint of the flexible metal−organic framework MIL-53(Al) using a combined experimental/computational approach. *J. Phys. Chem. C* **2018**, *122*, 2734−2746.

(21) Hoffman, A. E. J.; Senkovska, I.; Wieme, J.; Krylov, A.; Kaskel, S.; Van Speybroeck, V. Unfolding the terahertz spectrum of soft porous crystals: rigid unit modes and their impact on phase transitions. *J. Mater. Chem. A* **2022**, *10*, 17254−17266.

(22) Green, M. A.; Ho-Baillie, A.; Snaith, H. J. The emergence of perovskite solar cells. *Nat. photonics* **2014**, *8*, 506−514.

(23) Seok, S. I.; Grätzel, M.; Park, N.-G. Methodologies toward highly efficient perovskite solar cells. *Small* **2018**, *14*, 1704177.

(24) Correa-Baena, J.-P.; Saliba, M.; Buonassisi, T.; Grätzel, M.; Abate, A.; Tress, W.; Hagfeldt, A. Promises and challenges of perovskite solar cells. *Science* **2017**, *358*, 739−744.
(25) Pandey, R.; Vats, G.; Yun, J.; Bowen, C. R.; Ho-Baillie, A. W.; Seidel, J.; Butler, K. T.; Seok, S. I. Mutual insight on ferroelectrics and hybrid halide perovskites: a platform for future multifunctional energy conversion. *Adv. Mater.* **2019**, *31*, 1807376.
(26) Buurmans, I. L. C.; Weckhuysen, B. M. Heterogeneities of individual catalyst particles in space and time as monitored by spectroscopy. *Nat. Chem.* **2012**, *4*, 873−886.
(27) Howarth, A. J.; Peters, A. W.; Vermeulen, N. A.; Wang, T. C.; Hupp, J. T.; Farha, O. K. Best practices for the synthesis, activation, and characterization of metal−organic frameworks. *Chem. Mater.* **2017**, *29*, 26−39.
(28) Bon, V.; Brunner, E.; Pöppl, A.; Kaskel, S. Unraveling structure and dynamics in porous frameworks via advanced in situ characterization techniques. *Adv. Funct. Mater.* **2020**, *30*, 1907847.
(29) Kim, M.-c.; Ham, S.-Y.; Cheng, D.; Wynn, T. A.; Jung, H. S.; Meng, Y. S. Advanced characterization techniques for overcoming challenges of perovskite solar cell materials. *Adv. Energy Mater.* **2021**, *11*, 2001753.
(30) Bordiga, S.; Lamberti, C.; Bonino, F.; Travert, A.; Thibault-Starzyk, F. Probing zeolites by vibrational spectroscopies. *Chem. Soc. Rev.* **2015**, *44*, 7262−7341.
(31) Brivio, F.; Frost, J. M.; Skelton, J. M.; Jackson, A. J.; Weber, O. J.; Weller, M. T.; Goni, A. R.; Leguy, A. M. A.; Barnes, P. R. F.; Walsh, A. Lattice dynamics and vibrational spectra of the orthorhombic, tetragonal, and cubic phases of methylammonium lead iodide. *Phys. Rev. B* **2015**, *92*, 144308.
(32) Hadjiivanov, K. I.; Panayotov, D. A.; Mihaylov, M. Y.; Ivanova, E. Z.; Chakarova, K. K.; Andonova, S. M.; Drenchev, N. L. Power of infrared and Raman spectroscopies to characterize metal−organic frameworks and investigate their interaction with guest molecules. *Chem. Rev.* **2021**, *121*, 1286−1424.
(33) Walker, A. M.; Civalleri, B.; Slater, B.; Mellot-Draznieks, C.; Corà, F.; Zicovich-Wilson, C. M.; Román-Pérez, G.; Soler, J. M.; Gale, J. D. Flexibility in a metal−organic framework material controlled by weak dispersion forces: the bistability of MIL-53 (Al). *Angew. Chem., Int. Ed.* **2010**, *49*, 7501−7503.
(34) Wieme, J.; Lejaeghere, K.; Kresse, G.; Van Speybroeck, V. Tuning the balance between dispersion and entropy to design temperature-responsive flexible metal-organic frameworks. *Nat. Commun.* **2018**, *9*, 4899.
(35) Butler, K. T.; Svane, K.; Kieslich, G.; Cheetham, A. K.; Walsh, A. Microscopic origin of entropy-driven polymorphism in hybrid organic-inorganic perovskite materials. *Phys. Rev. B* **2016**, *94*, 180103.
(36) Butler, K. T.; Vervoorts, P.; Ehrenreich, M. G.; Armstrong, J.; Skelton, J. M.; Kieslich, G. Experimental evidence for vibrational entropy as driving parameter of flexibility in the metal−organic framework ZIF-4(Zn). *Chem. Mater.* **2019**, *31*, 8366−8372.
(37) Ehrling, S.; Senkovska, I.; Efimova, A.; Bon, V.; Abylgazina, L.; Petkov, P.; Evans, J. D.; Gamal Attallah, A.; Wharmby, M. T.; Roslova, M.; Huang, Z.; Tanaka, H.; Wagner, A.; Schmidt, P.; Kaskel, S. Temperature Driven Transformation of the Flexible Metal−Organic Framework DUT-8 (Ni). *Chem. Eur. J.* **2022**, *28*, No. e202201281.
(38) Hanna, L.; Lockard, J. V. From IR to x-rays: gaining molecular level insights on metal-organic frameworks through spectroscopy. *J. Phys.: Condens. Matter* **2019**, *31*, 483001.
(39) Lambert, A. G.; Davies, P. B.; Neivandt, D. J. Implementing the theory of sum frequency generation vibrational spectroscopy: A tutorial review. *Appl. Spectrosc. Rev.* **2005**, *40*, 103−145.
(40) Cheng, Y. Q.; Daemen, L. L.; Kolesnikov, A. I.; Ramirez-Cuesta, A. J. Simulation of inelastic neutron scattering spectra using OCLIMAX. *J. Chem. Theory Comput.* **2019**, *15*, 1974−1982.
(41) Ryder, M. R.; Civalleri, B.; Bennett, T. D.; Henke, S.; Rudić, S.; Cinque, G.; Fernandez-Alonso, F.; Tan, J.-C. Identifying the role of terahertz vibrations in metal-organic frameworks: from gate-opening phenomenon to shear-driven structural destabilization. *Phys. Rev. Lett.* **2014**, *113*, 215502.
(42) Ruggiero, M. T. Invited review: Modern methods for accurately simulating the terahertz spectra of solids. *J. Infrared Millim. Terahertz Waves* **2020**, *41*, 491−528.
(43) Yost, B. T.; Gibbons, B.; Wilson, A.; Morris, A. J.; McNeil, L. E. Vibrational spectroscopy investigation of defects in Zr-and Hf-UiO-66. *RSC Adv.* **2022**, *12*, 22440−22447.
(44) Lezcano-Gonzalez, I.; Campbell, E.; Hoffman, A. E. J.; Bocus, M.; Sazanovich, I. V.; Towrie, M.; Agote-Aran, M.; Gibson, E. K.; Greenaway, A.; De Wispelaere, K.; Van Speybroeck, V.; Beale, A. M. Insight into the effects of confined hydrocarbon species on the lifetime of methanol conversion catalysts. *Nat. Mater.* **2020**, *19*, 1081−1087.
(45) Kuchta, B.; Formalik, F.; Rogacka, J.; Neimark, A. V.; Firlej, L. Phonons in deformable microporous crystalline solids. *Z. Kristallogr. Cryst. Mater.* **2019**, *234*, 513−527.
(46) Gentile, F. S.; Pannico, M.; Causà, M.; Mensitieri, G.; Di Palma, G.; Scherillo, G.; Musto, P. Metal defects in HKUST-1 MOF revealed by vibrational spectroscopy: A combined quantum mechanical and experimental study. *J. Mater. Chem. A* **2020**, *8*, 10796−10812.
(47) Chibani, S.; Chiter, F.; Cantrel, L.; Paul, J.-F. Capture of iodine species in MIL-53(Al), MIL-120(Al), and HKUST-1(Cu) periodic DFT and ab-initio molecular dynamics studies. *J. Phys. Chem. C* **2017**, *121*, 25283−25291.
(48) Manookian, B.; Hernandez, E. D.; Baer, M. D.; Mundy, C. J.; Jentoft, F. C.; Auerbach, S. M. Experimental and DFT Calculated IR Spectra of Guests in Zeolites: Acyclic Olefins and Host−Guest Interactions. *J. Phys. Chem. C* **2020**, *124*, 10561−10572.
(49) Van Speybroeck, V. Challenges in modelling dynamic processes in realistic nanostructured materials at operating conditions. *Philos. Trans. R. Soc. A* **2023**, *381*, 20220239.
(50) Togo, A.; Tanaka, I. First principles phonon calculations in materials science. *Scr. Mater.* **2015**, *108*, 1−5.
(51) Erba, A.; Maul, J.; Ferrabone, M.; Carbonnière, P.; Rérat, M.; Dovesi, R. Anharmonic vibrational states of solids from DFT calculations. Part I: Description of the potential energy surface. *J. Chem. Theory Comput.* **2019**, *15*, 3755−3765.
(52) Erba, A.; Maul, J.; Ferrabone, M.; Dovesi, R.; Rérat, M.; Carbonnière, P. Anharmonic vibrational states of solids from DFT calculations. Part II: Implementation of the VSCF and VCI methods. *J. Chem. Theory Comput.* **2019**, *15*, 3766−3777.
(53) Mouvet, F.; Villard, J.; Bolnykh, V.; Rothlisberger, U. Recent Advances in First-Principles Based Molecular Dynamics. *Acc. Chem. Res.* **2022**, *55*, 221−230.
(54) Thomas, M.; Brehm, M.; Fligg, R.; Vöhringer, P.; Kirchner, B. Computing vibrational spectra from ab initio molecular dynamics. *Phys. Chem. Chem. Phys.* **2013**, *15*, 6608−6622.
(55) Baroni, S.; Giannozzi, P.; Isaev, E. Density-functional perturbation theory for quasi-harmonic calculations. *Rev. Mineral. Geochem.* **2010**, *71*, 39−57.
(56) Huang, L.-F.; Lu, X.-Z.; Tennessen, E.; Rondinelli, J. M. An efficient ab-initio quasiharmonic approach for the thermodynamics of solids. *Comput. Mater. Sci.* **2016**, *120*, 84−93.
(57) Wilson, E. B.; Decius, J. C.; Cross, P. C. *Molecular vibrations: The theory of infrared and Raman vibrational spectra*; Dover Publications: New York, NY, 1980.
(58) Shen, Y. R. Surface properties probed by second-harmonic and sum-frequency generation. *Nature* **1989**, *337*, 519−525.
(59) Shen, Y. R. Basic theory of surface sum-frequency generation. *J. Phys. Chem. C* **2012**, *116*, 15505−15509.
(60) Loiseau, T.; Serre, C.; Huguenard, C.; Fink, G.; Taulelle, F.; Henry, M.; Bataille, T.; Férey, G. A rationale for the large breathing of the porous aluminum terephthalate (MIL-53) upon hydration. *Chem. Eur. J.* **2004**, *10*, 1373−1382.
(61) Cavka, J. H.; Jakobsen, S.; Olsbye, U.; Guillou, N.; Lamberti, C.; Bordiga, S.; Lillerud, K. P. A new zirconium inorganic building brick forming metal organic frameworks with exceptional stability. *J. Am. Chem. Soc.* **2008**, *130*, 13850−13851.

https://doi.org/10.1021/acs.jctc.3c00942
J. Chem. Theory Comput. 2024, 20, 513−531

(62) Stoumpos, C. C.; Malliakas, C. D.; Peters, J. A.; Liu, Z.; Sebastian, M.; Im, J.; Chasapis, T. C.; Wibowo, A. C.; Chung, D. Y.; Freeman, A. J.; Wessels, B. W.; Kanatzidis, M. G. Crystal growth of the perovskite semiconductor $CsPbBr_3$: a new material for high-energy radiation detection. *Cryst. Growth Des.* **2013**, *13*, 2722−2727.
(63) Hoffman, A. E. J.; Saha, R. A.; Borgmans, S.; Puech, P.; Braeckevelt, T.; Roeffaers, M. B. J.; Steele, J. A.; Hofkens, J.; Van Speybroeck, V. Understanding the phase transition mechanism in the lead halide perovskite CsPbBr3 via theoretical and experimental GIWAXS and Raman spectroscopy. *APL Materials* **2023**, *11*, 041124.
(64) Born, M.; Oppenheimer, R. Zur Quantentheorie der Molekeln. *Annalen der Physik* **1927**, *389*, 457−484.
(65) Harrison, J. A.; Schall, J. D.; Maskey, S.; Mikulski, P. T.; Knippenberg, M. T.; Morrow, B. H. Review of force fields and intermolecular potentials used in atomistic computational materials research. *Applied Physics Reviews* **2018**, *5*, 031104.
(66) Marzari, N.; Ferretti, A.; Wolverton, C. Electronic-structure methods for materials design. *Nat. Mater.* **2021**, *20*, 736−749.
(67) Lin, H.; Truhlar, D. G. QM/MM: what have we learned, where are we, and where do we go from here? *Theor. Chem. Acc.* **2007**, *117*, 185−199.
(68) Schleder, G. R.; Padilha, A. C.; Acosta, C. M.; Costa, M.; Fazzio, A. From DFT to machine learning: recent approaches to materials science−a review. *J. Phys. Mater.* **2019**, *2*, 032001.
(69) Mardirossian, N.; Head-Gordon, M. Thirty years of density functional theory in computational chemistry: an overview and extensive assessment of 200 density functionals. *Mol. Phys.* **2017**, *115*, 2315−2372.
(70) Verma, P.; Truhlar, D. G. Status and challenges of density functional theory. *Trends Chem.* **2020**, *2*, 302−318.
(71) Hasnip, P. J.; Refson, K.; Probert, M. I. J.; Yates, J. R.; Clark, S. J.; Pickard, C. J. Density functional theory in the solid state. *Philos. Trans. R. Soc. A* **2014**, *372*, 20130270.
(72) Prentice, J. C.; Aarons, J.; Womack, J. C.; Allen, A. E.; Andrinopoulos, L.; Anton, L.; Bell, R. A.; Bhandari, A.; Bramley, G. A.; Charlton, R. J.; Clements, R. J.; Cole, D. J.; Constantinescu, G.; Corsetti, F.; Dubois, S. M. M.; Duff, K. K. B.; Escartín, J. M.; Greco, A.; Hill, Q.; Lee, L. P.; Linscott, E.; O'Regan, D. D.; Phipps, M. J. S.; Ratcliff, L. E.; Serrano, A. R.; Tait, E. W.; Teobaldi, G.; Vitale, V.; Yeung, N.; Zuehlsdorff, T. J.; Dziedzic, J.; Haynes, P. D.; Hine, N. D. M.; Mostofi, A. A.; Payne, M. C.; Skylaris, C.-K. The ONETEP linear-scaling density functional theory program. *J. Chem. Phys.* **2020**, *152*, 174111.
(73) Chang, C.; Deringer, V. L.; Katti, K. S.; Van Speybroeck, V.; Wolverton, C. M. Simulations in the era of exascale computing. *Nat. Rev. Mater.* **2023**, *8*, 309−313.
(74) Jorgensen, W. L.; Maxwell, D. S.; Tirado-Rives, J. Development and testing of the OPLS all-atom force field on conformational energetics and properties of organic liquids. *J. Am. Chem. Soc.* **1996**, *118*, 11225−11236.
(75) Wang, J.; Wolf, R. M.; Caldwell, J. W.; Kollman, P. A.; Case, D. A. Development and testing of a general amber force field. *J. Comput. Chem.* **2004**, *25*, 1157−1174.
(76) Oostenbrink, C.; Villa, A.; Mark, A. E.; Van Gunsteren, W. F. A biomolecular force field based on the free enthalpy of hydration and solvation: the GROMOS force-field parameter sets 53A5 and 53A6. *J. Comput. Chem.* **2004**, *25*, 1656−1676.
(77) Vanommeslaeghe, K.; Hatcher, E.; Acharya, C.; Kundu, S.; Zhong, S.; Shim, J.; Darian, E.; Guvench, O.; Lopes, P.; Vorobyov, I.; Mackerell, A. D., Jr. CHARMM general force field: A force field for drug-like molecules compatible with the CHARMM all-atom additive biological force fields. *J. Comput. Chem.* **2010**, *31*, 671−690.
(78) Warshel, A.; Kato, M.; Pisliakov, A. V. Polarizable force fields: history, test cases, and prospects. *J. Chem. Theory Comput.* **2007**, *3*, 2034−2045.
(79) Cieplak, P.; Dupradeau, F.-Y.; Duan, Y.; Wang, J. Polarization effects in molecular mechanical force fields. *J. Phys.: Condens. Matter* **2009**, *21*, 333102.
(80) Jing, Z.; Liu, C.; Cheng, S. Y.; Qi, R.; Walker, B. D.; Piquemal, J.-P.; Ren, P. Polarizable force fields for biomolecular simulations: Recent advances and applications. *Annu. Rev. Biophys.* **2019**, *48*, 371.
(81) Cools-Ceuppens, M.; Dambre, J.; Verstraelen, T. Modeling electronic response properties with an explicit-electron machine learning potential. *J. Chem. Theory Comput.* **2022**, *18*, 1672−1691.
(82) Behler, J. First principles neural network potentials for reactive simulations of large molecular and condensed systems. *Angew. Chem., Int. Ed.* **2017**, *56*, 12828−12840.
(83) Butler, K. T.; Davies, D. W.; Cartwright, H.; Isayev, O.; Walsh, A. Machine learning for molecular and materials science. *Nature* **2018**, *559*, 547−555.
(84) Schmidt, J.; Marques, M. R. G.; Botti, S.; Marques, M. A. L. Recent advances and applications of machine learning in solid-state materials science. *npj Comput. Mater.* **2019**, *5*, 83.
(85) Keith, J. A.; Vassilev-Galindo, V.; Cheng, B.; Chmiela, S.; Gastegger, M.; Müller, K.-R.; Tkatchenko, A. Combining machine learning and computational chemistry for predictive insights into chemical systems. *Chem. Rev.* **2021**, *121*, 9816−9872.
(86) Brockherde, F.; Vogt, L.; Li, L.; Tuckerman, M. E.; Burke, K.; Müller, K.-R. Bypassing the Kohn-Sham equations with machine learning. *Nat. Commun.* **2017**, *8*, 872.
(87) Grisafi, A.; Fabrizio, A.; Meyer, B.; Wilkins, D. M.; Corminboeuf, C.; Ceriotti, M. Transferable machine-learning model of the electron density. *ACS Cent. Sci.* **2019**, *5*, 57−64.
(88) Chandrasekaran, A.; Kamal, D.; Batra, R.; Kim, C.; Chen, L.; Ramprasad, R. Solving the electronic structure problem with machine learning. *npj Comput. Mater.* **2019**, *5*, 22.
(89) Allen, R. E.; De Wette, F. W. Calculation of dynamical surface properties of noble-gas crystals. I. The quasiharmonic approximation. *Phys. Rev.* **1969**, *179*, 873.
(90) Erba, A.; Maul, J.; Civalleri, B. Thermal properties of molecular crystals through dispersion-corrected quasi-harmonic ab initio calculations: the case of urea. *Chem. Commun.* **2016**, *52*, 1820−1823.
(91) Christiansen, O.; Luis, J. M. Beyond vibrational self-consistent-field methods: Benchmark calculations for the fundamental vibrations of ethylene. *Int. J. Quantum Chem.* **2005**, *104*, 667−680.
(92) Roy, T. K.; Gerber, R. B. Vibrational self-consistent field calculations for spectroscopy of biological molecules: new algorithmic developments and applications. *Phys. Chem. Chem. Phys.* **2013**, *15*, 9468−9492.
(93) Piccini, G.; Sauer, J. Effect of anharmonicity on adsorption thermodynamics. *J. Chem. Theory Comput.* **2014**, *10*, 2479−2487.
(94) Bowman, J. M. Self-consistent field energies and wavefunctions for coupled oscillators. *J. Chem. Phys.* **1978**, *68*, 608−610.
(95) Gerber, R. B.; Ratner, M. A. A semiclassical self-consistent field (SC SCF) approximation for eigenvalues of coupled-vibration systems. *Chem. Phys. Lett.* **1979**, *68*, 195−198.
(96) Bowman, J. M.; Christoffel, K.; Tobin, F. Application of SCF-SI theory to vibrational motion in polyatomic molecules. *J. Phys. Chem.* **1979**, *83*, 905−912.
(97) Carbonnière, P.; Dargelos, A.; Pouchan, C. The VCI-P code: an iterative variation−perturbation scheme for efficient computations of anharmonic vibrational levels and IR intensities of polyatomic molecules. *Theor. Chem. Acc.* **2010**, *125*, 543−554.
(98) Norris, L. S.; Ratner, M. A.; Roitberg, A. E.; Gerber, R. B. Møller−Plesset perturbation theory applied to vibrational problems. *J. Chem. Phys.* **1996**, *105*, 11261−11267.
(99) Chaban, G. M.; Jung, J. O.; Gerber, R. B. Ab initio calculation of anharmonic vibrational states of polyatomic systems: Electronic structure combined with vibrational self-consistent field. *J. Chem. Phys.* **1999**, *111*, 1823−1829.
(100) Christiansen, O. Møller−Plesset perturbation theory for vibrational wave functions. *J. Chem. Phys.* **2003**, *119*, 5773−5781.
(101) Christiansen, O. A second quantization formulation of multimode dynamics. *J. Chem. Phys.* **2004**, *120*, 2140−2148.
(102) Christiansen, O. Vibrational coupled cluster theory. *J. Chem. Phys.* **2004**, *120*, 2149−2159.

https://doi.org/10.1021/acs.jctc.3c00942
J. Chem. Theory Comput. 2024, 20, 513−531

(103) Martyna, G. J.; Klein, M. L.; Tuckerman, M. Nosé−Hoover chains: The canonical ensemble via continuous dynamics. *J. Chem. Phys.* **1992**, *97*, 2635−2643.
(104) Martyna, G. J.; Tobias, D. J.; Klein, M. L. Constant pressure molecular dynamics algorithms. *J. Chem. Phys.* **1994**, *101*, 4177−4189.
(105) Kühne, T. D.; Iannuzzi, M.; Del Ben, M.; Rybkin, V. V.; Seewald, P.; Stein, F.; Laino, T.; Khaliullin, R. Z.; Schütt, O.; Schiffmann, F.; Golze, D.; Wilhelm, J.; Chulkov, S.; Bani-Hashemian, M. H.; Weber, V.; Borštnik, U.; Taillefumier, M.; Jakobovits, A. S.; Lazzaro, A.; Pabst, H.; Müller, T.; Schade, R.; Guidon, M.; Andermatt, S.; Holmberg, N.; Schenter, G. K.; Hehn, A.; Bussy, A.; Belleflamme, F.; Tabacchi, G.; Glöß, A.; Lass, M.; Bethune, I.; Mundy, C. J.; Plessl, C.; Watkins, M.; VandeVondele, J.; Krack, M.; Hutter, J. CP2K: An electronic structure and molecular dynamics software package - Quickstep: Efficient and accurate electronic structure calculations. *J. Chem. Phys.* **2020**, *152*, 194103.
(106) Gaigeot, M.-P.; Martinez, M.; Vuilleumier, R. Infrared spectroscopy in the gas and liquid phase from first principle molecular dynamics simulations: application to small peptides. *Mol. Phys.* **2007**, *105*, 2857−2878.
(107) Markland, T. E.; Ceriotti, M. Nuclear quantum effects enter the mainstream. *Nat. Rev. Chem.* **2018**, *2*, 0109.
(108) Resta, R. Macroscopic polarization in crystalline dielectrics: the geometric phase approach. *Rev. Mod. Phys.* **1994**, *66*, 899.
(109) Giannozzi, P.; De Gironcoli, S.; Pavone, P.; Baroni, S. Ab initio calculation of phonon dispersions in semiconductors. *Phys. Rev. B* **1991**, *43*, 7231.
(110) Ramírez, R.; López-Ciudad, T.; Kumar P, P.; Marx, D. Quantum corrections to classical time-correlation functions: Hydrogen bonding and anharmonic floppy modes. *J. Chem. Phys.* **2004**, *121*, 3973−3983.
(111) Gonze, X.; Rignanese, G.-M.; Caracas, R. First-principle studies of the lattice dynamics of crystals, and related properties. *Z. Krist. Cryst. Mater.* **2005**, *220*, 458−472.
(112) Sternheimer, R. M. Electronic polarizabilities of ions from the Hartree-Fock wave functions. *Phys. Rev.* **1954**, *96*, 951.
(113) Luber, S.; Iannuzzi, M.; Hutter, J. Raman spectra from ab initio molecular dynamics and its application to liquid S-methyloxirane. *J. Chem. Phys.* **2014**, *141*, 094503.
(114) Perdew, J. P.; Burke, K.; Ernzerhof, M. Generalized gradient approximation made simple. *Phys. Rev. Lett.* **1996**, *77*, 3865.
(115) Grimme, S.; Antony, J.; Ehrlich, S.; Krieg, H. A consistent and accurate ab initio parametrization of density functional dispersion correction (DFT-D) for the 94 elements H-Pu. *J. Chem. Phys.* **2010**, *132*, 154104.
(116) Grimme, S.; Ehrlich, S.; Goerigk, L. Effect of the damping function in dispersion corrected density functional theory. *J. Comput. Chem.* **2011**, *32*, 1456−1465.
(117) Kresse, G.; Hafner, J. Ab initio molecular dynamics for liquid metals. *Phys. Rev. B* **1993**, *47*, 558.
(118) Kresse, G.; Furthmüller, J. Efficiency of ab-initio total energy calculations for metals and semiconductors using a plane-wave basis set. *Comput. Mater. Sci.* **1996**, *6*, 15−50.
(119) Kresse, G.; Furthmüller, J. Efficient iterative schemes for ab initio total-energy calculations using a plane-wave basis set. *Phys. Rev. B* **1996**, *54*, 11169.
(120) Rogge, S. M. J.; Wieme, J.; Vanduyfhuys, L.; Vandenbrande, S.; Maurin, G.; Verstraelen, T.; Waroquier, M.; Van Speybroeck, V. Thermodynamic insight in the high-pressure behavior of UiO-66: Effect of linker defects and linker expansion. *Chem. Mater.* **2016**, *28*, 5721−5732.
(121) Blöchl, P. E. Projector augmented-wave method. *Phys. Rev. B* **1994**, *50*, 17953.
(122) Monkhorst, H. J.; Pack, J. D. Special points for Brillouin-zone integrations. *Phys. Rev. B* **1976**, *13*, 5188.
(123) Vanpoucke, D. E. P.; Lejaeghere, K.; Van Speybroeck, V.; Waroquier, M.; Ghysels, A. Mechanical properties from periodic plane wave quantum mechanical codes: the challenge of the flexible nanoporous MIL-47(V) framework. *J. Phys. Chem. C* **2015**, *119*, 23752−23766.
(124) Lippert, G.; Hutter, J.; Parrinello, M. A hybrid Gaussian and plane wave density functional scheme. *Mol. Phys.* **1997**, *92*, 477−488.
(125) VandeVondele, J.; Hutter, J. Gaussian basis sets for accurate calculations on molecular systems in gas and condensed phases. *J. Chem. Phys.* **2007**, *127*, 114105.
(126) Goedecker, S.; Teter, M.; Hutter, J. Separable dual-space Gaussian pseudopotentials. *Phys. Rev. B* **1996**, *54*, 1703.
(127) Ruggiero, M. T.; Zhang, W.; Bond, A. D.; Mittleman, D. M.; Zeitler, J. A. Uncovering the connection between low-frequency dynamics and phase transformation phenomena in molecular solids. *Phys. Rev. Lett.* **2018**, *120*, 196002.
(128) Liu, Y.; Her, J.-H.; Dailly, A.; Ramirez-Cuesta, A. J.; Neumann, D. A.; Brown, C. M. Reversible structural transition in MIL-53 with large temperature hysteresis. *J. Am. Chem. Soc.* **2008**, *130*, 11813−11818.
(129) Yot, P. G.; Boudene, Z.; Macia, J.; Granier, D.; Vanduyfhuys, L.; Verstraelen, T.; Van Speybroeck, V.; Devic, T.; Serre, C.; Férey, G.; Stock, N.; Maurin, G. Metal−organic frameworks as potential shock absorbers: the case of the highly flexible MIL-53(Al). *Chem. Commun.* **2014**, *50*, 9462−9464.
(130) Boutin, A.; Springuel-Huet, M.-A.; Nossov, A.; Gedeon, A.; Loiseau, T.; Volkringer, C.; Férey, G.; Coudert, F.-X.; Fuchs, A. H. Breathing transitions in MIL-53(Al) metal−organic framework upon xenon adsorption. *Angew. Chem., Int. Ed.* **2009**, *48*, 8314−8317.
(131) Hoffman, A. E. J.; Wieme, J.; Rogge, S. M. J.; Vanduyfhuys, L.; Van Speybroeck, V. The impact of lattice vibrations on the macroscopic breathing behavior of MIL-53(Al). *Z. Kristallogr. Cryst. Mater.* **2019**, *234*, 529−545.
(132) Serre, C.; Bourrelly, S.; Vimont, A.; Ramsahye, N. A.; Maurin, G.; Llewellyn, P. L.; Daturi, M.; Filinchuk, Y.; Leynaud, O.; Barnes, P.; Férey, G. An explanation for the very large breathing effect of a metal−organic framework during CO_2 adsorption. *Adv. Mater.* **2007**, *19*, 2246−2251.
(133) Hamon, L.; Llewellyn, P. L.; Devic, T.; Ghoufi, A.; Clet, G.; Guillerm, V.; Pirngruber, G. D.; Maurin, G.; Serre, C.; Driver, G.; van Beek, W.; Jolimaître, E.; Vimont, A.; Daturi, M.; Férey, G. Co-adsorption and separation of CO_2-CH_4 mixtures in the highly flexible MIL-53(Cr) MOF. *J. Am. Chem. Soc.* **2009**, *131*, 17490−17499.
(134) Kloutse, F. A.; Zacharia, R.; Cossement, D.; Chahine, R. Specific heat capacities of MOF-5, Cu-BTC, Fe-BTC, MOF-177 and MIL-53(Al) over wide temperature ranges: Measurements and application of empirical group contribution method. *Microporous Mesoporous Mater.* **2015**, *217*, 1−5.
(135) Yot, P. G.; Yang, K.; Ragon, F.; Dmitriev, V.; Devic, T.; Horcajada, P.; Serre, C.; Maurin, G. Exploration of the mechanical behavior of metal organic frameworks UiO-66(Zr) and MIL-125(Ti) and their NH_2 functionalized versions. *Dalton Trans* **2016**, *45*, 4283−4288.
(136) Burtch, N. C.; Baxter, S. J.; Heinen, J.; Bird, A.; Schneemann, A.; Dubbeldam, D.; Wilkinson, A. P. Negative thermal expansion design strategies in a diverse series of metal−organic frameworks. *Adv. Funct. Mater.* **2019**, *29*, 1904669.
(137) Luo, J.-P.; Zhang, J.; Yin, N.; Wang, T.-P.; Tan, Z.-C.; Han, W.; Shi, Q. An experimental strategy for evaluating the energy performance of metal−organic framework-based carbon dioxide adsorbents. *Chem. Eng. J.* **2022**, *442*, 136210.
(138) Rakita, Y.; Cohen, S. R.; Kedem, N. K.; Hodes, G.; Cahen, D. Mechanical properties of $APbX_3$ (A= Cs or CH_3NH_3; X= I or Br) perovskite single crystals. *MRS Commun.* **2015**, *5*, 623−629.
(139) Haeger, T.; Heiderhoff, R.; Riedl, T. Thermal properties of metal-halide perovskites. *J. Mater. Chem. C* **2020**, *8*, 14289−14311.
(140) Evarestov, R. A.; Kotomin, E. A.; Senocrate, A.; Kremer, R. K.; Maier, J. First-principles comparative study of perfect and defective $CsPbX_3$ (X= Br, I) crystals. *Phys. Chem. Chem. Phys.* **2020**, *22*, 3914−3920.
(141) Woodcock, D. A.; Lightfoot, P.; Villaescusa, L. A.; Díaz-Cabañas, M.-J.; Camblor, M. A.; Engberg, D. Negative thermal

expansion in the siliceous zeolites chabazite and ITQ-4: A neutron powder diffraction study. *Chem. Mater.* **1999**, *11*, 2508−2514.
(142) Fang, Z.; Bueken, B.; De Vos, D. E.; Fischer, R. A. Defect-engineered metal−organic frameworks. *Angew. Chem., Int. Ed.* **2015**, *54*, 7234−7254.
(143) Han, T.-H.; Tan, S.; Xue, J.; Meng, L.; Lee, J.-W.; Yang, Y. Interface and defect engineering for metal halide perovskite optoelectronic devices. *Adv. Mater.* **2019**, *31*, 1803515.
(144) Yan, X.; Liu, C.; Gadre, C. A.; Gu, L.; Aoki, T.; Lovejoy, T. C.; Dellby, N.; Krivanek, O. L.; Schlom, D. G.; Wu, R.; Pan, X. Single-defect phonons imaged by electron microscopy. *Nature* **2021**, *589*, 65−69.
(145) Wu, H.; Yildirim, T.; Zhou, W. Exceptional mechanical stability of highly porous zirconium metal−organic framework UiO-66 and its important implications. *J. Phys. Chem. Lett.* **2013**, *4*, 925−930.
(146) Shearer, G. C.; Chavan, S.; Bordiga, S.; Svelle, S.; Olsbye, U.; Lillerud, K. P. Defect engineering: tuning the porosity and composition of the metal−organic framework UiO-66 via modulated synthesis. *Chem. Mater.* **2016**, *28*, 3749−3761.
(147) Bueken, B.; Van Velthoven, N.; Krajnc, A.; Smolders, S.; Taulelle, F.; Mellot-Draznieks, C.; Mali, G.; Bennett, T. D.; De Vos, D. Tackling the defect conundrum in UiO-66: a mixed-linker approach to engineering missing linker defects. *Chem. Mater.* **2017**, *29*, 10478−10486.
(148) Cliffe, M. J.; Wan, W.; Zou, X.; Chater, P. A.; Kleppe, A. K.; Tucker, M. G.; Wilhelm, H.; Funnell, N. P.; Coudert, F.-X.; Goodwin, A. L. Correlated defect nanoregions in a metal−organic framework. *Nat. Commun.* **2014**, *5*, 4176.
(149) Chavan, S. M.; Shearer, G. C.; Svelle, S.; Olsbye, U.; Bonino, F.; Ethiraj, J.; Lillerud, K. P.; Bordiga, S. Synthesis and characterization of amine-functionalized mixed-ligand metal−organic frameworks of UiO-66 topology. *Inorg. Chem.* **2014**, *53*, 9509−9515.
(150) Cavalcante, L. S.; Dettmann, M. A.; Sours, T.; Yang, D.; Daemen, L. L.; Gates, B. C.; Kulkarni, A. R.; Moulé, A. J. Elucidating correlated defects in metal organic frameworks using theory-guided inelastic neutron scattering spectroscopy. *Mater. Horiz.* **2023**, *10*, 187−196.
(151) Shearer, G. C.; Chavan, S.; Ethiraj, J.; Vitillo, J. G.; Svelle, S.; Olsbye, U.; Lamberti, C.; Bordiga, S.; Lillerud, K. P. Tuned to perfection: ironing out the defects in metal−organic framework UiO-66. *Chem. Mater.* **2014**, *26*, 4068−4071.
(152) Marronnier, A.; Lee, H.; Geffroy, B.; Even, J.; Bonnassieux, Y.; Roma, G. Structural instabilities related to highly anharmonic phonons in halide perovskites. *J. Phys. Chem. Lett.* **2017**, *8*, 2659−2665.
(153) Marronnier, A.; Roma, G.; Boyer-Richard, S.; Pedesseau, L.; Jancu, J.-M.; Bonnassieux, Y.; Katan, C.; Stoumpos, C. C.; Kanatzidis, M. G.; Even, J. Anharmonicity and disorder in the black phases of cesium lead iodide used for stable inorganic perovskite solar cells. *ACS Nano* **2018**, *12*, 3477−3486.
(154) Quarti, C.; Mosconi, E.; Ball, J. M.; D'Innocenzo, V.; Tao, C.; Pathak, S.; Snaith, H. J.; Petrozza, A.; De Angelis, F. Structural and optical properties of methylammonium lead iodide across the tetragonal to cubic phase transition: implications for perovskite solar cells. *Energy Environ. Sci.* **2016**, *9*, 155−163.
(155) Yaffe, O.; Guo, Y.; Tan, L. Z.; Egger, D. A.; Hull, T.; Stoumpos, C. C.; Zheng, F.; Heinz, T. F.; Kronik, L.; Kanatzidis, M. G.; Owen, J. S.; Rappe, A. M.; Pimenta, M. A.; Brus, L. E. Local polar fluctuations in lead halide perovskite crystals. *Phys. Rev. Lett.* **2017**, *118*, 136001.
(156) Yang, R. X.; Skelton, J. M.; Da Silva, E. L.; Frost, J. M.; Walsh, A. Spontaneous octahedral tilting in the cubic inorganic cesium halide perovskites $CsSnX_3$ and $CsPbX_3$ (X= F, Cl, Br, I). *J. Phys. Chem. Lett.* **2017**, *8*, 4720−4726.
(157) Filip, M. R.; Eperon, G. E.; Snaith, H. J.; Giustino, F. Steric engineering of metal-halide perovskites with tunable optical band gaps. *Nat. Commun.* **2014**, *5*, 5757.
(158) Whitcher, T. J.; Gomes, L. C.; Zhao, D.; Bosman, M.; Chi, X.; Wang, Y.; Carvalho, A.; Hui, H. K.; Chang, Q.; Breese, M. B. H.; Castro Neto, A. H.; Wee, A. T. S.; Sun, H. D.; Chia, E. E. M.; Rusydi, A. Dual phases of crystalline and electronic structures in the nanocrystalline perovskite CsPbBr3. *NPG Asia Mater.* **2019**, *11*, 70.
(159) Olsbye, U.; Svelle, S.; Bjørgen, M.; Beato, P.; Janssens, T. V. W.; Joensen, F.; Bordiga, S.; Lillerud, K. P. Conversion of methanol to hydrocarbons: how zeolite cavity and pore size controls product selectivity. *Angew. Chem., Int. Ed.* **2012**, *51*, 5810−5831.
(160) Hemelsoet, K.; Van der Mynsbrugge, J.; De Wispelaere, K.; Waroquier, M.; Van Speybroeck, V. Unraveling the reaction mechanisms governing methanol-to-olefins catalysis by theory and experiment. *ChemPhysChem* **2013**, *14*, 1526−1545.
(161) Van Speybroeck, V.; De Wispelaere, K.; Van der Mynsbrugge, J.; Vandichel, M.; Hemelsoet, K.; Waroquier, M. First principle chemical kinetics in zeolites: the methanol-to-olefin process as a case study. *Chem. Soc. Rev.* **2014**, *43*, 7326−7357.
(162) Matam, S. K.; Nastase, S. A. F.; Logsdail, A. J.; Catlow, C. R. A. Methanol loading dependent methoxylation in zeolite H-ZSM-5. *Chem. Sci.* **2020**, *11*, 6805−6814.
(163) Lightfoot, P.; Woodcock, D. A.; Maple, M. J.; Villaescusa, L. A.; Wright, P. A. The widespread occurrence of negative thermal expansion in zeolites. *J. Mater. Chem.* **2001**, *11*, 212−216.

https://doi.org/10.1021/acs.jctc.3c00942
J. Chem. Theory Comput. 2024, 20, 513−531